Hybrid-Encoding-Based Reverse Time Migration of Multiples

Baoqing Tian, Feng Hu, Yanbao Zhang, Yike Liu, Ning Wang, *Member, IEEE*, and Jing Sun

***Abstract*—Multiples propagate along longer paths than primaries and have been incorporated into reverse time migration (RTM) to enhance subsurface illumination. However, RTM of multiples often suffers from severe crosstalk artifacts caused by cross-correlations among unrelated multiple orders. Moreover, the conventional shot-domain RTM framework becomes computationally expensive when a large number of shots are involved. To address these challenges, we propose a hybrid-encoding-based RTM method for multiple imaging. Different multiple orders are first separated using a decomposition technique. Random-phase encoding is then applied to consecutive-order multiples to form supergathers, and linear time-delay encoding is used to compress these supergathers into a limited number of plane-wave gathers. The multiple-based image is subsequently obtained using the RTM operator. Compared with conventional shot-domain RTM of multiples, the proposed plane-wave-domain approach effectively suppresses crosstalk from chaotic-order interference while substantially reducing computational cost. Numerical experiments on the Pluto 1.5 model demonstrate that the method efficiently attenuates coherent crosstalk and improves the imaging of complex subsurface structures.**

***Index Terms*—Computational efficiency, crosstalk attenuation, hybrid encoding, imaging with multiples, reverse time migration (RTM).**

I. Introduction

Seismic data acquired in field surveys contain various reflections generated at interfaces with strong acoustic impedance contrasts, such as the free surface, the seafloor, and salt boundaries. Among these events, primary reflections are waves that travel from the source to a subsurface reflector and return directly to the receivers without interacting with the free surface. In addition to primaries, seismic records also include multiple reflections, which undergo extra round trips between the free surface and subsurface interfaces. Traditionally, multiples have been treated as coherent noise and removed before migration using methods such as surface-related multiple elimination (SRME) [1], [2] or Radon-transform-based techniques [3], [4]. However, because multiples propagate along different paths from primaries, they carry complementary structural information and can illuminate areas that are poorly sampled by primaries. In recent years, this insight has motivated a shift from suppressing multiples to exploiting them as useful signals. Many studies have shown that incorporating multiples into seismic imaging can significantly improve subsurface illumination and enhance structural resolution [5], [6], [7], [8], [9], [10], [11], [12], [13], [14], [15], [16], [17].

Among seismic imaging methods, reverse time migration (RTM) reconstructs the full wavefield by solving the two-way wave equation. It has demonstrated strong capability for imaging complex subsurface structures [18], [19], [20], [21], [22]. To further exploit the information carried by multiples, Liu et al. [9] proposed the RTM of multiples (RTMMs). This method extends the RTM framework by explicitly incorporating multiples into the imaging process. In RTMM, the original seismic data, which contain both primaries and multiples, are treated as an areal source distributed over all receiver locations. These data are forward propagated to generate the source-side wavefield. At the same time, the multiples are backward propagated to construct the receiver-side wavefield. Applying an imaging condition to these two wavefields yields an image of subsurface reflectivity associated with multiples.

Crosstalk artifacts remain a major challenge that limits the practical application of multiple imaging. During migration with multiples, only interactions between consecutive multiple orders contribute constructively to the final image. For example, forward-propagating first-order multiples correlate coherently with backward-propagating second-order multiples. The order of multiples is defined by the number of reflections at the free surface. In contrast, interactions among nonconsecutive or unrelated orders generate strong crosstalk artifacts. These artifacts obscure true reflectivity and degrade image quality. Liu et al. [23] categorized these artifacts into multiple-type and irregular-type components. Zhang et al. [24] further classified them as order-related and event-related components, induced by the sequence and interaction of different orders. To suppress coherent crosstalk artifacts, an order-to-order migration strategy has been proposed. In this approach, multiples of different orders are first separated using a multiple-decomposition technique. Each order is then migrated independently to ensure order consistency. By avoiding cross-correlations among disordered multiple orders, this strategy effectively attenuates crosstalk artifacts and produces high-quality images [25], [26], [27]. However, this benefit comes at a high computational cost. The total cost increases

Received 7 November 2025; revised 17 December 2025 and 17 January 2026; accepted 21 January 2026. Date of publication 26 January 2026; date of current version 6 February 2026. This work was supported in part by the National Natural Science Foundation of China under Grant 42374075 and Grant 42130807; and in part by the Deep Earth Probe and Mineral Resources Exploration, National Science and Technology Major Project of China under Grant 2024ZD1000307. *(Corresponding authors: Yanbao Zhang; Ning Wang.)*

Baoqing Tian and Yanbao Zhang are with the Institute of Geophysics, China Earthquake Administration, Beijing 100081, China, and also with Beijing Baijiatuan Earth Sciences National Observation and Research Station, Beijing 100095, China (e-mail: tianbaoqing@cea-igp.ac.cn; ybzhang@cea-igp.ac.cn).

Feng Hu is with Zhejiang Institute of Communications Company Ltd., Hangzhou 310030, China (e-mail: hufeng_zjic@163.com).

Yike Liu is with the Key Laboratory of Deep Petroleum Intelligent Exploration and Development, Institute of Geology and Geophysics, Chinese Academy of Sciences, Beijing 100029, China (e-mail: ykliu@mail.iggcas.ac.cn).

Ning Wang is with the School of Earth Sciences, Northeast Petroleum University, Daqing 163318, China (e-mail: wangn2311@163.com).

Jing Sun is with the Intelligent Systems Department, Delft University of Technology, 2628 XE Delft, The Netherlands (e-mail: Jing.Sun@tudelft.nl).

Digital Object Identifier 10.1109/TGRS.2026.3657835

by a factor of N_m, where N_m is the number of multiple orders included in the imaging process.

Conventional migration is usually performed on a shot-by-shot basis. As a result, its computational cost scales linearly with the number of shots. For RTM, this demand becomes a major obstacle in large-scale industrial applications. To reduce the cost, random-phase encoding has been introduced. This technique uses random time shifts and polarity reversals to combine a number of shot gathers for simultaneous migration [28], [29], [30]. However, it is generally limited to fixed-spread acquisition geometries [31], [32], [33]. Despite this limitation, random-phase encoding can be adapted to multiple imaging. Specifically, N_m orders of multiples can be combined into supergathers because the source-side jth-order multiples share receiver locations with the receiver-side $(j+1)$th-order multiples. Under this configuration, the computational cost of the order-to-order migration can be reduced to a level comparable to conventional shot-domain RTM [34], [35], [36]. Even so, the overall cost remains high for practical applications.

Plane-wave migration offers another effective alternative to enhance efficiency. It transforms hundreds of shot gathers into a smaller number of coherent plane-wave gathers [37], [38], [39], [40]. This approach applies linear time-delay encoding to different shots, and each plane-wave gather corresponds to a specific take-off angle. Compared with random-phase encoding, plane-wave encoding is better suited to flexible acquisition geometries [41], [42], [43], such as marine towed-streamer surveys. However, plane-wave encoding alone does not suppress multiple-related crosstalk artifacts [44]. In summary, neither random-phase encoding nor plane-wave encoding by itself can achieve both high efficiency and effective crosstalk suppression in multiple imaging. This motivates the development of a new strategy that delivers images with a high signal-to-noise ratio (SNR) while remaining computationally practical.

The remainder of this article is organized as follows. We first review previous studies on seismic imaging using multiples. We then develop the proposed hybrid-encoding-based approach by integrating random-phase and plane-wave encodings. Next, numerical experiments based on the Pluto 1.5 model are presented to evaluate the feasibility and effectiveness of the method. Finally, we discuss the results and summarize the main conclusions.

II. Method

A. Basic Principles of RTMM

According to the adjoint-state method [45], conventional RTM involves two finite-difference simulations: one for the source-side wavefield

$$\left(\frac{1}{v^2(\mathbf{x})}\frac{\partial^2}{\partial t^2} - \nabla^2\right) P_0(\mathbf{x}, t; s) = f(t; s), \tag{1}$$

and another for the receiver-side wavefield

$$\left(\frac{1}{v^2(\mathbf{x})}\frac{\partial^2}{\partial t^2} - \nabla^2\right) Q_0(\mathbf{x}, t; s) = g_0(\mathbf{x}_r, t; s) \tag{2}$$

where $\mathbf{x}_r$ denotes the receiver position, s denotes the shot index, $v(\mathbf{x})$ represents the background velocity model used for migration, t is the wave propagation time, g_0 refers to a shot gather containing only primaries, and $f(t; s)$ denotes the point source. The source-side wavefield P_0 propagates forward in time, whereas the receiver-side wavefield Q_0 propagates backward in time. The single-shot migration image of primaries is obtained by applying a zero-lag cross-correlation imaging condition

$$R_0(\mathbf{x}; s) = \sum_t P_0(\mathbf{x}, t; s) Q_0(\mathbf{x}, t; s). \tag{3}$$

The conventional RTM operator is derived under the assumption that the recorded data contain only primaries. It neglects the valuable information carried by multiples. To migrate multiples with the RTM operator, Liu et al. [9] replaced the point source with the original data g to generate the source-side wavefield P

$$\left(\frac{1}{v^2(\mathbf{x})}\frac{\partial^2}{\partial t^2} - \nabla^2\right) P(\mathbf{x}, t; s) = g(\mathbf{x}_r, t; s), \tag{4}$$

and treat the estimated multiples g_m as the boundary condition to construct the receiver-side wavefield Q

$$\left(\frac{1}{v^2(\mathbf{x})}\frac{\partial^2}{\partial t^2} - \nabla^2\right) Q(\mathbf{x}, t; s) = g_m(\mathbf{x}_r, t; s). \tag{5}$$

Then, the imaging condition for RTMM can be expressed as follows:

$$R_m(\mathbf{x}; s) = \sum_t P(\mathbf{x}, t; s) Q(\mathbf{x}, t; s) \tag{6}$$

where $R_m(\mathbf{x}; s)$ denotes the single-shot migration image of multiples. According to the definition of multiple order, the two wavefields in (6) can be decomposed into components of different orders

$$\begin{cases} P(\mathbf{x}, t; s) = \sum_{j=0}^{N_m} P_j(\mathbf{x}, t; s) \\ Q(\mathbf{x}, t; s) = \sum_{k=1}^{N_m} Q_k(\mathbf{x}, t; s) \end{cases} \tag{7}$$

where N_m represents the maximum order of multiples, P_j denotes the source-side wavefield that recovers the image of the $(j+1)$th-order multiples, and Q_k denotes the receiver-side wavefield that rebuilds the image of the kth-order multiples. During wavefield extrapolation, the simulated wavefields are not perfectly terminated as expected, resulting in complex cross-correlations. As demonstrated by Liu et al. [9], cross-correlations between consecutive-order multiples contribute constructively to the final image, whereas those between nonconsecutive orders generate undesirable crosstalk artifacts. Substituting (7) into (6) yields an expanded form of the imaging condition

$$\begin{aligned} R_m(\mathbf{x}; s) &= \sum_t P(\mathbf{x}, t; s)\, Q(\mathbf{x}, t; s) \\ &= \sum_t \left[\sum_{j=0}^{N_m} P_j(\mathbf{x}, t; s)\right]\left[\sum_{k=1}^{N_m} Q_k(\mathbf{x}, t; s)\right] \\ &= \sum_t \sum_{j=0}^{N_m} \sum_{k=1}^{N_m} P_j(\mathbf{x}, t; s)\, Q_k(\mathbf{x}, t; s) \\ &= \sum_t \Bigg[\underbrace{\sum_{j=0}^{N_m-1} P_j(\mathbf{x}, t; s)\, Q_{j+1}(\mathbf{x}, t; s)}_{\text{signal}} \\ &\quad + \underbrace{\sum_{j=0}^{N_m} \sum_{\substack{k=1 \\ k \neq j+1}}^{N_m} P_j(\mathbf{x}, t; s)\, Q_k(\mathbf{x}, t; s)}_{\text{crosstalk}} \Bigg]. \end{aligned} \tag{8}$$

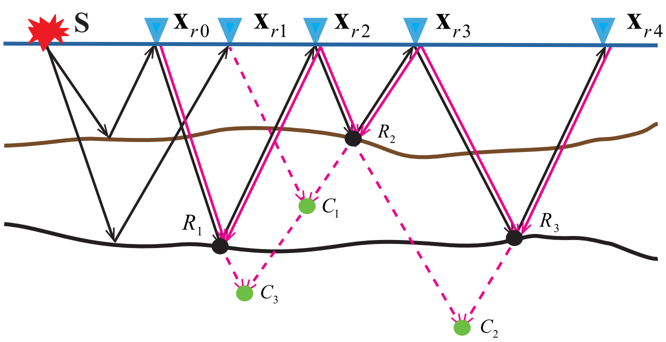

Fig. 1. Ray-path diagrams illustrating imaging points and crosstalk artifacts in RTMM. Black circles indicate true imaging points, whereas green circles denote crosstalk artifacts.

Fig. 1 depicts several representative points within the RTMM process. To recover the first-order image, the forward-propagating primary $S \rightarrow \mathbf{x}_{r0}$ is cross-correlated at the imaging point R_1 with the backward-extrapolating first-order multiple $S \rightarrow \mathbf{x}_{r0} \rightarrow \mathbf{x}_{r2}$. Similarly, when the first-order multiple $S \rightarrow \mathbf{x}_{r0} \rightarrow \mathbf{x}_{r2}$ (or the second-order multiple at $\mathbf{x}_{r3}$) is treated as a virtual source for the second-order multiple $S \rightarrow \mathbf{x}_{r0} \rightarrow \mathbf{x}_{r2} \rightarrow \mathbf{x}_{r3}$ (or the third-order multiple at $\mathbf{x}_{r4}$), the interaction between these wavefields forms the imaging point R_2 (or R_3) for the second-order (or the third-order) image. When reconstructing the first-order image, the forward-extrapolated primary $S \rightarrow \mathbf{x}_{r0}$ or $S \rightarrow \mathbf{x}_{r1}$ also cross-correlates with the backward-propagated second-order multiple $S \rightarrow \mathbf{x}_{r0} \rightarrow \mathbf{x}_{r2} \rightarrow \mathbf{x}_{r3}$ at crosstalk points C_3 or C_1. In addition, the anticausal interaction between the first-order multiple $S \rightarrow \mathbf{x}_{r0} \rightarrow \mathbf{x}_{r2}$ and the third-order multiple recorded at $\mathbf{x}_{r4}$ produces another crosstalk point C_2.

B. Consecutive-Order RTMM

Crosstalk artifacts severely degrade migration images and represent a major challenge for multiple-based imaging. To address this, Liu et al. [25] proposed the consecutive-order RTMM (C-RTMM). In this approach, multiples of different orders are first extracted and then migrated in an order-to-order manner. For a single shot, the final image is obtained by stacking the migration results from all individual orders. The imaging condition of C-RTMM can be expressed as follows:

$$R_c(\mathbf{x}; s) = \sum_{j=0}^{N_m-1} \sum_t P_j(\mathbf{x}, t; s) Q_{j+1}(\mathbf{x}, t; s). \tag{9}$$

By reversing the order of summation, the imaging condition becomes equivalent to the signal term in (8). For a dataset containing N_s shots, the final image is obtained by accumulating all single-shot images

$$R_c(\mathbf{x}) = \sum_{s=1}^{N_s} \sum_{j=0}^{N_m-1} \sum_t P_j(\mathbf{x}, t; s) Q_{j+1}(\mathbf{x}, t; s). \tag{10}$$

C-RTMM differs from RTMM in several key aspects. It replaces the original seismic data with a specific-order multiple as the secondary source and uses the one-order-higher multiple as the boundary condition. These changes decompose the original complex wavefield into a series of order-dependent components. As a result, C-RTMM eliminates the crosstalk term in (8) and improves crosstalk suppression. However, a comparison of the imaging condition in (9) with those of RTM (3) and RTMM (6) reveals a major drawback. C-RTMM requires N_m independent migrations, resulting in a calculation cost that is approximately N_m times that of RTM or RTMM.

C. Phase-Encoding-Based RTMM

To improve the computational efficiency of C-RTMM, Liu et al. [34] and Zhang and Liu [35] incorporated random-phase encoding into RTMM. The random-phase encoding function consists of two components. The first is a time shift following a standard normal distribution. The second is a sign function that represents polarity reversal and takes values of 1 or −1 with equal probability 1/2

$$\begin{cases} \tau_j^s \sim N(0, \sigma^2) \\ \mathrm{sign}(\tau_j^s) \end{cases} \quad s = 1, 2, \ldots, N_s \tag{11}$$

where τ_j^s denotes the time shift applied to the jth-order multiple in the sth shot, and σ is the standard deviation, which is selected to be greater than the dominant period of the source wavelet [29]. Multiples of different orders are then phase-encoded randomly and combined into supergathers as follows:

$$\begin{cases} g_f(\mathbf{x}_r, t; s) = \sum_{j=0}^{N_m-1} \mathrm{sign}(\tau_j^s) g_j(\mathbf{x}_r, t + \tau_j^s; s) \\ g_b(\mathbf{x}_r, t; s) = \sum_{k=0}^{N_m-1} \mathrm{sign}(\tau_k^s) g_{k+1}(\mathbf{x}_r, t + \tau_k^s; s) \end{cases} \tag{12}$$

where g_f and g_b represent the forward-injected and backward-extrapolated supergathers for the sth shot, respectively.

After the encoding and stacking process described in (12), the phase-encoding-based RTMM (PE-RTMM) method is formulated, and its imaging condition is expressed as follows:

$$R_{\mathrm{pe}}(\mathbf{x}) = \sum_{s=1}^{N_s} \sum_t \hat{P}(\mathbf{x}, t; s) \hat{Q}(\mathbf{x}, t; s) \tag{13}$$

where $\hat{P}$ denotes the source-side wavefield, and $\hat{Q}$ represents the receiver-side wavefield. Furthermore, we investigate (13) by decomposing wavefields into different orders

$$\begin{aligned} R_{\mathrm{pe}}(\mathbf{x}) &= \sum_{s=1}^{N_s} \sum_t \left(\sum_{j=0}^{N_m-1} \hat{P}_j^s\right) \left(\sum_{k=0}^{N_m-1} \hat{Q}_{k+1}^s\right) \\ &= \underbrace{\sum_{s=1}^{N_s} \sum_t \sum_{j=0}^{N_m-1} \hat{P}_j^s \hat{Q}_{j+1}^s}_{\text{signal}} \\ &\quad + \underbrace{\sum_{s=1}^{N_s} \sum_t \left(\sum_{j=0}^{N_m-1} \hat{P}_j^s\right) \left(\sum_{k=0, k \neq j}^{N_m-1} \hat{Q}_{k+1}^s\right)}_{\text{random noise}} \\ &= R_c(\mathbf{x}) + \text{random noise} \end{aligned} \tag{14}$$

where $\hat{P}_j^s$ represents the source-side wavefield generated by forward propagation of the encoded jth-order multiple, and $\hat{Q}_{k+1}^s$ represents the receiver-side wavefield obtained by backward propagation of the encoded $(k+1)$th-order multiple. The cross-correlation between two encoded consecutive-order wavefields, $\hat{P}_j^s$ and $\hat{Q}_{j+1}^s$, is equivalent to that between their unencoded counterparts, P_j and Q_{j+1}, because both wavefields share identical time shifts and polarity reversals. By exchanging the order of the last two summations, it can be shown that

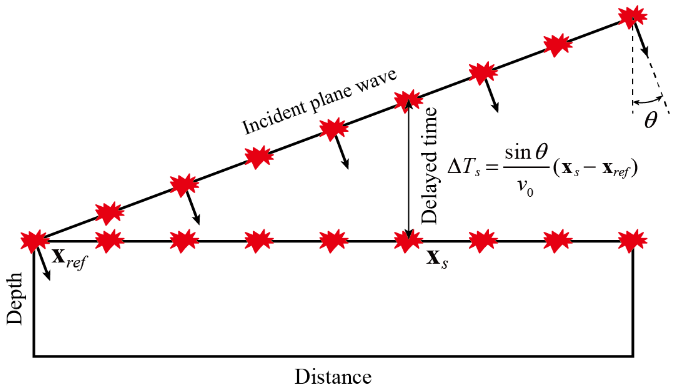

Fig. 2. Schematic illustration of plane-wave encoding, where the time delay ΔT_s varies linearly with the source position $\mathbf{x}_s$.

the signal term corresponds exactly to the imaging condition of C-RTMM in (10). All other encoded wavefield pairs use different phase encoding functions and constitute the random noise term in (14), where the random-phase encoding causes the wavefields to interfere destructively [29], [35].

The PE-RTMM method uses phase-encoded supergathers to image all N_m orders of multiples simultaneously. This approach reduces the computational cost to a level comparable to that of conventional RTM or RTMM. At the same time, it preserves the crosstalk-suppression capability of C-RTMM. Moreover, the random noise term introduced by phase encoding does not contain the coherent artifacts that characterize the crosstalk term of (8). A comparison of (14) against (8) and (10) indicates that PE-RTMM produces higher quality images than RTMM, although its performance remains slightly inferior to that of C-RTMM.

Despite these advantages, PE-RTMM is still implemented in the shot domain. Each supergather is migrated independently and then stacked. Consequently, $2N_s$ wavefield simulations are required, comprising N_s source-side wavefield extrapolations and N_s receiver-side wavefield extrapolations. As the total number of shots increases, the computational cost of such shot-domain migration grows rapidly.

D. Plane-Wave RTMM

Plane-wave migration provides an efficient alternative for subsurface imaging by transforming a large set of shot gathers into a smaller set of plane-wave gathers. In this and Section II-E, we perform multiple-based migrations in the plane-wave domain to significantly reduce the computational cost of the shot-domain migrations. For imaging with multiples in the plane-wave domain, the plane-wave gathers are constructed as follows:

$$\begin{cases} g_f(\mathbf{x}_r, t; \xi_i) = \sum_{s=1}^{N_s} g(\mathbf{x}_r, t; s) * \delta(t - \xi_i(\mathbf{x}_s - \mathbf{x}_{ref})) \\ g_b(\mathbf{x}_r, t; \xi_i) = \sum_{u=1}^{N_s} g_m(\mathbf{x}_r, t; u) * \delta(t - \xi_i(\mathbf{x}_u - \mathbf{x}_{ref})) \end{cases} \quad (15)$$

where $\mathbf{x}_s$, $\mathbf{x}_u$, and $\mathbf{x}_{ref}$ denote the spatial position of the sth shot, the uth shot, and the reference point, respectively. A time-delay encoding function, $\delta(t - \xi_i(\mathbf{x}_s - \mathbf{x}_{ref}))$, is applied to the shot gathers of both the original data and the estimated multiples to generate plane-wave gathers $g_f(\mathbf{x}_r, t; \xi_i)$ and $g_b(\mathbf{x}_r, t; \xi_i)$. As illustrated in Fig. 2, the time delay $\xi_i(\mathbf{x}_s - \mathbf{x}_{ref})$ is a linear function of the source position $\mathbf{x}_s$ [38], and ξ_i represents the ray parameter defined as follows:

$$\xi_i = \frac{\sin\theta}{v_0} \quad (16)$$

where the subscript i denotes the ray-parameter index, θ is the surface take-off angle, and v_0 is the velocity at the surface.

It should be noted that applying time delays to shot gathers is equivalent to applying the same time delays to the corresponding wavefields. Accordingly, the source-side and receiver-side wavefields in the plane-wave domain can be expressed as the summation of their shot-domain counterparts

$$\begin{cases} P(\mathbf{x}, t; \xi_i) = \sum_{s=1}^{N_s} P(\mathbf{x}, t - \xi_i(\mathbf{x}_s - \mathbf{x}_{ref}); s) \\ Q(\mathbf{x}, t; \xi_i) = \sum_{u=1}^{N_s} Q(\mathbf{x}, t - \xi_i(\mathbf{x}_u - \mathbf{x}_{ref}); u) \end{cases}. \quad (17)$$

The zero-lag cross-correlation imaging condition is then applied to generate an image corresponding to a single take-off angle. For all N_i plane-wave gathers, the plane-wave RTMM (PW-RTMM) procedure can be formulated as follows:

$$R_{pw}(\mathbf{x}) = \sum_{i=1}^{N_i} \sum_t P(\mathbf{x}, t; \xi_i) Q(\mathbf{x}, t; \xi_i). \quad (18)$$

Substituting (17) into (18) and then decomposing wavefields into different-order components yields the expanded form of the imaging condition

$$R_{pw}(\mathbf{x}) = \sum_{i=1}^{N_i} \sum_t \Bigg[\underbrace{\sum_{j=0}^{N_m-1} P_j(\mathbf{x}, t; \xi_i) Q_{j+1}(\mathbf{x}, t; \xi_i)}_{\text{signal}} + \underbrace{\sum_{\substack{j=0 \\ k \neq j+1}} P_j(\mathbf{x}, t; \xi_i) Q_k(\mathbf{x}, t; \xi_i)}_{\text{crosstalk}} \Bigg] \quad (19)$$

where $P_j(\mathbf{x}, t; \xi_i) = \sum_{s=1}^{N_s} P_j(\mathbf{x}, t - \xi_i(\mathbf{x}_s - \mathbf{x}_{ref}); s)$ and $Q_k(\mathbf{x}, t; \xi_i) = \sum_{u=1}^{N_s} Q_k(\mathbf{x}, t - \xi_i(\mathbf{x}_u - \mathbf{x}_{ref}); u)$ denote the source-side and receiver-side wavefields, respectively. Both wavefields are associated with the ray parameter ξ_i. The crosstalk term remains coherent because it originates from nonconsecutive-order multiples, analogous to the crosstalk term in (8).

E. Hybrid-Encoding-Based RTMM

By encoding hundreds of shot gathers (N_s) into only dozens of plane-wave gathers (N_i), PW-RTMM improves computational efficiency by a factor of N_s/N_i. However, similar to conventional RTMM, PW-RTMM cannot effectively suppress crosstalk generated by nonconsecutive-order multiples. In contrast, PE-RTMM can image all N_m orders of multiples simultaneously while retaining the crosstalk-suppression capability of C-RTMM. Nevertheless, because PE-RTMM is formulated in the shot domain, it still entails substantial computational cost. Consequently, neither random-phase encoding nor plane-wave encoding alone can simultaneously achieve high computational efficiency and effective crosstalk suppression.

To simultaneously achieve effective crosstalk suppression and enhanced computational efficiency, we propose a hybrid-encoding-based RTMM (HE-RTMM). In this method, multiples of individual orders are first phase-encoded into supergathers according to (12). Linear time-delay encoding functions are then applied to these supergathers to generate the corresponding plane-wave gathers

$$\begin{cases} g_{\rm sf}(\mathbf{x}_r,t;\xi_i) = \\ \quad \sum_{s=1}^{N_s}\sum_{j=0}^{N_m-1} \operatorname{sign}(\tau_j^s)\, g_j(\mathbf{x}_r, t-\xi_i(\mathbf{x}_s-\mathbf{x}_{\rm ref})+\tau_j^s; s) \\ g_{\rm sb}(\mathbf{x}_r,t;\xi_i) = \\ \quad \sum_{u=1}^{N_s}\sum_{j=0}^{N_m-1}\operatorname{sign}(\tau_j^u)\, g_{j+1}(\mathbf{x}_r, t-\xi_i(\mathbf{x}_u-\mathbf{x}_{\rm ref})+\tau_j^u;u)\end{cases} \tag{20}$$

where $g_{\rm sf}$ and $g_{\rm sb}$ denote the areal source and boundary condition for HE-RTMM, respectively. All other parameters in (20) are identical to those in (15). After simulating the source-side wavefield $P_{\rm sf}(\mathbf{x},t;\xi_i)$ and the receiver-side wavefield $Q_{\rm sb}(\mathbf{x},t;\xi_i)$, the image of HE-RTMM can be obtained using

$$R_{\rm he}(\mathbf{x}) = \sum_{i=1}^{N_i}\sum_t P_{\rm sf}(\mathbf{x},t;\xi_i)Q_{\rm sb}(\mathbf{x},t;\xi_i). \tag{21}$$

By decomposing $P_{\rm sf}$ and $Q_{\rm sb}$ into components of different orders, we have

$$\begin{cases} P_{\rm sf}(\mathbf{x},t;\xi_i) = \sum_{s=1}^{N_s}\sum_{j=0}^{N_m-1}\hat{P}_{j,i}^s \\ Q_{\rm sb}(\mathbf{x},t;\xi_i) = \sum_{u=1}^{N_s}\sum_{k=0}^{N_m-1}\hat{Q}_{k+1,i}^u \end{cases} \tag{22}$$

where $\hat{P}_{j,i}^s = \operatorname{sign}(\tau_j^s)P_j(\mathbf{x}, t-\xi_i(\mathbf{x}_s - x_{ref})+\tau_j^s; s)$ and $\hat{Q}_{k+1,i}^u = \operatorname{sign}(\tau_k^u)Q_{k+1}(\mathbf{x}, t-\xi_i(\mathbf{x}_u-\mathbf{x}_{ref})+\tau_k^u; u)$ denote the source-side and receiver-side wavefields, respectively. Substituting (22) into (21) yields the expanded imaging condition as follows:

$$\begin{aligned} R_{\rm he}(\mathbf{x}) &= \sum_{i=1}^{N_i}\sum_t\left(\sum_{s=1}^{N_s}\sum_{j=0}^{N_m-1}\hat{P}_{j,i}^s\right)\left(\sum_{u=1}^{N_s}\sum_{k=0}^{N_m-1}\hat{Q}_{k+1,i}^u\right) \\ &= \underbrace{\sum_{i=1}^{N_i}\sum_t\sum_{s=1}^{N_s}\sum_{j=0}^{N_m-1}\hat{P}_{j,i}^s\hat{Q}_{j+1,i}^s}_{\text{signal}} \\ &\quad + \underbrace{\sum_{i=1}^{N_i}\sum_t\left(\sum_{s=1}^{N_s}\sum_{j=0}^{N_m-1}\hat{P}_{j,i}^s\right)\left(\sum_{u=1}^{N_s}\sum_{k=0,k\neq j}^{N_m-1}\hat{Q}_{j+1,i}^u\right)}_{\text{random noise}}. \end{aligned} \tag{23}$$

When the range and number of ξ_i becomes sufficiently large, the relation $\sum_{i=1}^{N_i}\hat{P}_{j,i}^s\hat{Q}_{j+1,i}^s \approx P_j(\mathbf{x},t;s)Q_{j+1}(\mathbf{x},t;s)$ holds. By rearranging the summation order to follow the sequence s, j, t, and i, the signal term becomes approximately equivalent to the imaging condition of C-RTMM (10). Like the random noise term in (14), all other simulation pairs involving nonconsecutive orders are randomly encoded and therefore contribute to the random noise term. Therefore, we can obtain the approximate form of (23) as follows:

$$R_{\rm he}(\mathbf{x}) \overset{\substack{N_i\to\infty \\ \xi_i:-\infty\to+\infty}}{\approx} R_c(\mathbf{x}) + \text{random noise}. \tag{24}$$

F. Implementation of HE-RTMM

The proposed HE-RTMM integrates random-phase encoding with linear time-delay encoding to combine their respective advantages. Random-phase encoding enables effective suppression of multiple-related crosstalk, whereas the plane-wave formulation provides substantial computational efficiency. Based on the descriptions above, the workflow of the hybrid-encoding imaging methodology can be summarized as follows.

1) Decompose the original data $g(\mathbf{x}_r,t;s)$ into specific multiple orders $g_j(\mathbf{x}_r,t;s)$ using the multiple-decomposition procedure outlined in the Appendix.
2) Construct the forward and backward supergathers $g_f(\mathbf{x}_r,t;s)$ and $g_b(\mathbf{x}_r,t;s)$ using (12). In this step, different-order multiples are first randomly phase-encoded and then stacked. Importantly, identical phase-encoding functions are applied to the forward-propagating jth-order multiples and the backward-propagating $(j+1)$th-order multiples
3) Apply the linear time-delay encoding function in (20) to generate the plane-wave gathers $g_{\rm sf}(\mathbf{x}_r,t;\xi_i)$ and $g_{\rm sb}(\mathbf{x}_r,t;\xi_i)$.
4) Simulate the source-side and receiver-side wavefields by forward-propagating $g_{\rm sf}(\mathbf{x}_r,t;\xi_i)$ and backward-extrapolating $g_{\rm sb}(\mathbf{x}_r,t;\xi_i)$, respectively.
5) Form the multiple-based image $R_{\rm he}(\mathbf{x})$ by applying the imaging condition defined in (21).

The HE-RTMM implementation flowchart is illustrated in Fig. 3.

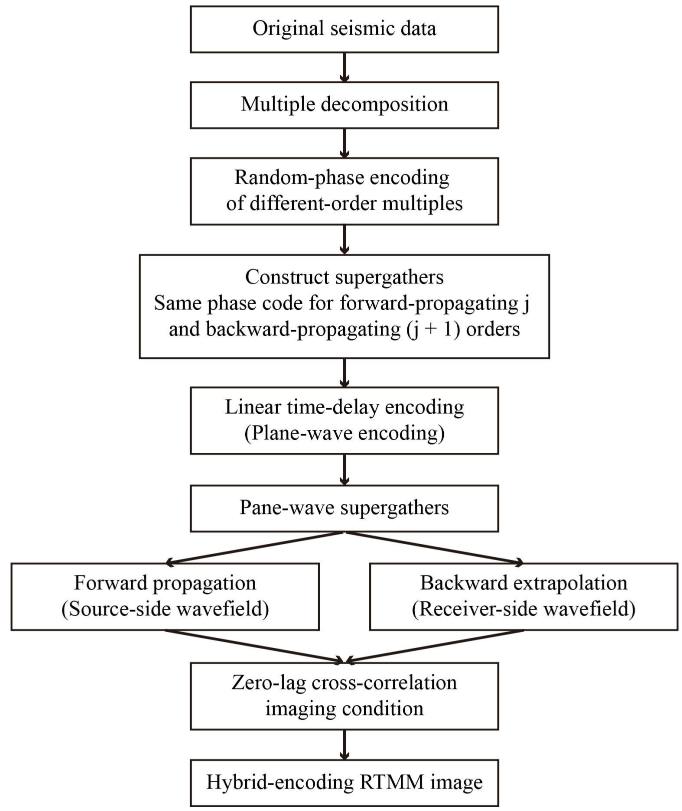

Fig. 3. Workflow of the proposed HE-RTMM.

III. Numerical Examples

In this section, we evaluate the performance of the proposed method using the 2-D Subsalt Multiples Attenuation and Reduction Team (SMAART) Pluto 1.5 dataset and its corresponding velocity model [46]. The released dataset contains 1387 shot gathers with a shot spacing of 22.86 m and has

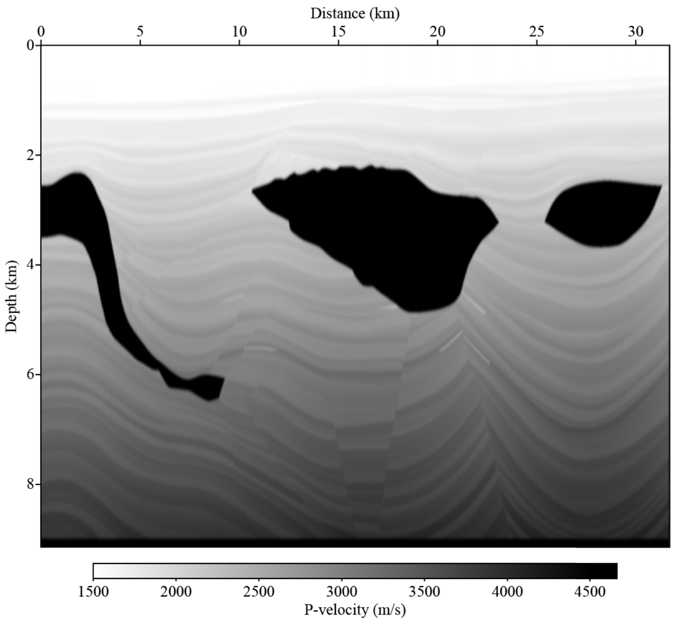

Fig. 4. Smoothed Pluto 1.5 velocity model used for migration.

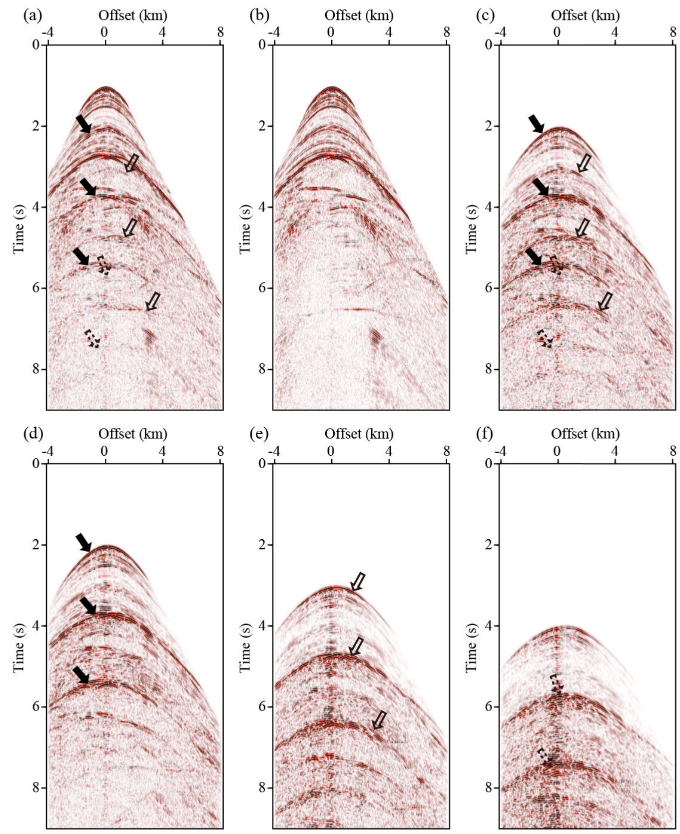

Fig. 5. Decomposition results of the Pluto 1.5 dataset obtained using the proposed workflow (a) original data, (b) primaries, (c) all-order multiples, (d) first-order multiples, (e) second-order multiples, and (f) third-order multiples. The black solid arrows in (d) [the hollow arrows in (e) or the dashed hollow arrows in (f)] indicate that the first-order (the second-order or the third-order) multiples are effectively isolated by the decomposition workflow.

been widely used to assess multiple-elimination algorithms. Each shot gather consists of 540 traces with a trace spacing of 22.86 m. The total recording time is 9 s, sampled at 8 ms intervals, and the source wavelet is a Ricker wavelet with a dominant frequency of 15 Hz.

Fig. 4 shows the migration velocity model, which was obtained by applying a three-point spatial median smoother to the true velocity model. The model is discretized on a grid of 1387 horizontal and 1201 vertical points, with grid spacings of 22.86 and 7.62 m, respectively. Because the computational cost of shot-domain migrations (i.e., RTM, RTMM, C-RTMM, and PE-RTMM) scales linearly with the number of shots, the original 1387 shot gathers were decimated by retaining every third shot, resulting in 463 shot gathers for migration experiments. During migration, both source-side and receiver-side wavefields were simulated using a staggered-grid finite-difference acoustic wave-equation solver.

A. Data Preparations for Different-Order Multiples

Before multiple-based imaging is performed, the original seismic data are decomposed into different multiple orders following the workflow described in the Appendix. Each multiple order is extracted using a prediction-and-subtraction strategy. In this procedure, multiples are first predicted with a feedback iteration model and then adaptively subtracted from the data in a least-squares sense.

Fig. 5 shows the decomposition results for the Pluto 1.5 dataset. As indicated by the arrows in Fig. 5(a), the original data contain a large amount of multiples extending from shallow to deep regions and spanning nearly the entire profile. These multiples strongly interfere with the primaries and significantly degrade the overall SNR of the data. Because the SNR of the input data directly affects the final image quality of the primaries, the predicted all-order multiples [Fig. 5(c)] are adaptively subtracted from the original data to obtain the primary-only data [Fig. 5(b)]. To isolate the first-order multiples, the primaries are convolved with the predicted all-order multiples to generate second-order and higher multiples. These higher order multiples are then subtracted from the all-order multiples, yielding the first-order multiples shown in Fig. 5(d). The black solid arrows indicate that only the first-order multiples remain, while higher order multiples are effectively suppressed. Using a similar procedure, the second-order multiples (Fig. 5(e), hollow arrows) and third-order multiples (Fig. 5(f), dashed hollow arrows) are sequentially separated from the remaining components. The decomposition results for the complex Pluto 1.5 dataset demonstrate that the proposed workflow can effectively and robustly isolate multiples of different orders.

B. Comparison of RTM, RTMM, and C-RTMM

To examine the imaging characteristics of primaries and multiples, we applied RTM, RTMM, and C-RTMM to the decomposed Pluto 1.5 dataset. Fig. 6(a) shows the imaging result obtained using primary-only RTM. The image is free of coherent crosstalk artifacts associated with multiples and therefore serves as a reference for evaluating the performance of multiple-based imaging methods. The RTMM result is shown in Fig. 6(b). Overall, RTMM delineates the sedimentary layers and salt boundaries as well as the RTM result. However, pronounced crosstalk artifacts are visible, as indicated by the arrows. These artifacts arise from cross-correlations between nonconsecutive multiple orders and significantly

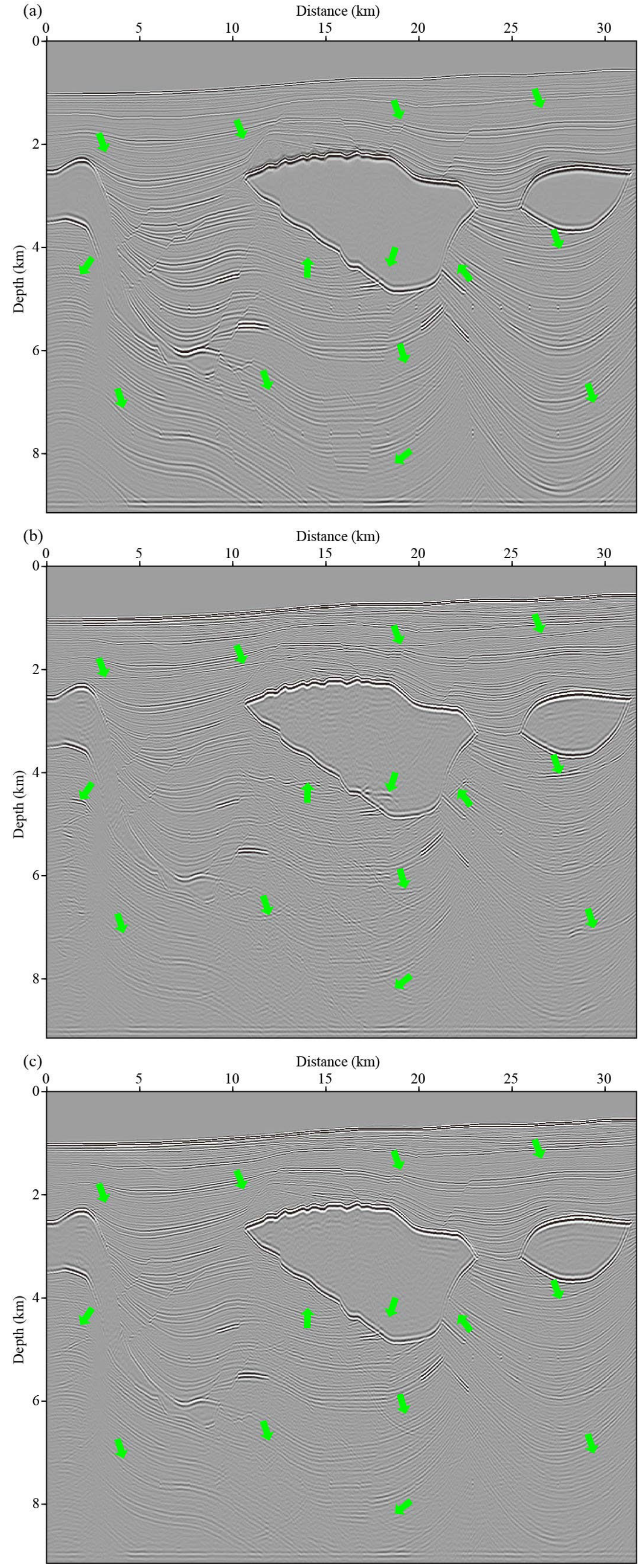

Fig. 6. Imaging results obtained using (a) conventional primary-only RTM, (b) RTMM, and (c) C-RTMM, where the latter two methods utilize multiples. The RTMM image in (b) exhibits artifacts, as indicated by the arrows, which are effectively suppressed by C-RTMM, as shown in (c).

distort the stratigraphic sequence. For example, the strong event approximately parallel to the seafloor, highlighted by the upper four arrows, originates from water-layer reverberations.

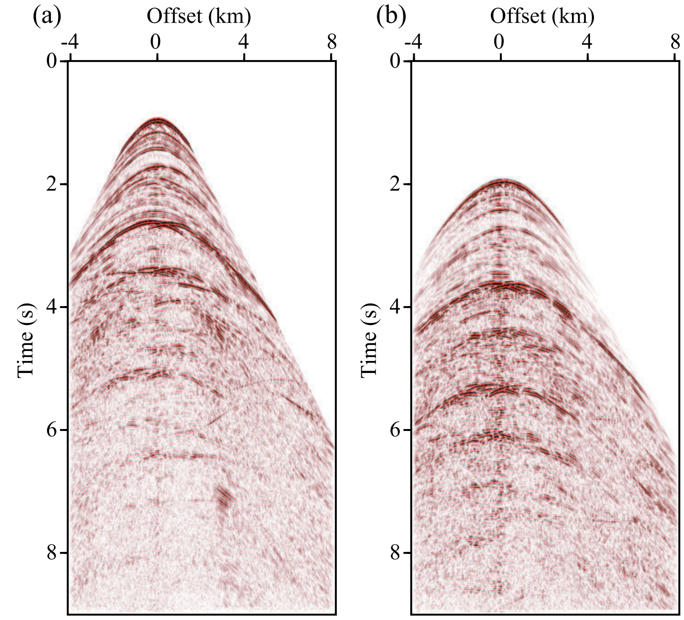

Fig. 7. Illustration of supergathers. (a) Forward-propagated supergather containing encoded primaries, first-order multiples, and second-order multiples. (b) Backward-propagated supergather containing encoded first-, second-, and third-order multiples.

This spurious interface laterally smears the shallow structures from left to right, which may lead to erroneous geological interpretations.

To suppress such crosstalk artifacts, the first-, second-, and third-order multiples were migrated independently and then stacked to form the C-RTMM image shown in Fig. 6(c). Compared with the RTM and RTMM results [Fig. 6(a) and (b)], C-RTMM effectively attenuates the crosstalk artifacts, including the event parallel to the seafloor, and yields improved structural resolution. This improvement, however, comes at a substantial computational cost. Because C-RTMM requires independent migration operators for each multiple order, its computational expense scales with the number of considered orders, N_m. In this example, imaging the first three multiple orders requires three times the computational cost of conventional RTM or RTMM.

C. Behavior of PE-RTMM

Applying PE-RTMM to phase-encoded supergathers enables the simultaneous migration of all N_m multiple orders, thereby substantially reducing the computational cost relative to C-RTMM. As defined in (12), the separated primaries and different-order multiples are randomly phase-encoded and stacked into supergathers. Consecutive orders are assigned identical time shifts and polarity reversals, whereas nonconsecutive orders receive independent random-phase encodings. This encoding strategy preserves coherent correlations between consecutive orders while randomizing crosstalk among nonconsecutive orders. Following the recommendation of Schuster et al. [29], the standard deviation of the temporal shifts should exceed the dominant period of the source wavelet. In this study, we selected a standard deviation equal to seven times the dominant period (0.467 s) to construct the encoding functions for the Pluto 1.5 dataset. Fig. 7 shows the resulting supergathers. One supergather [Fig. 7(a)] acts as a virtual

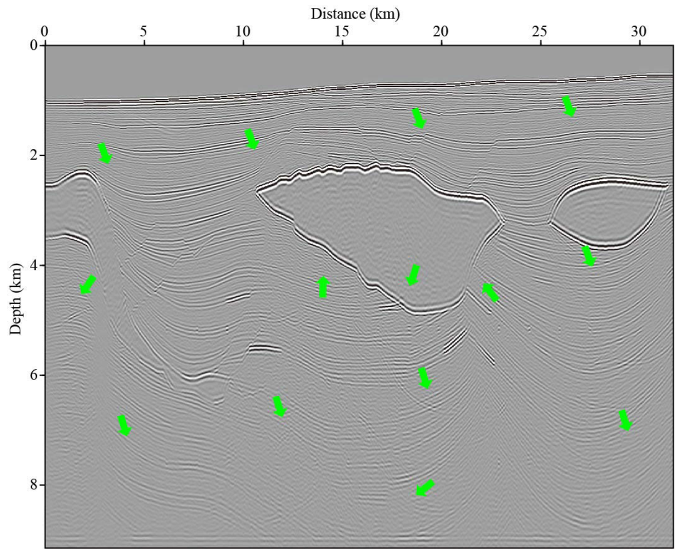

Fig. 8. Imaging result obtained using PE-RTMM. As indicated by the arrows, PE-RTMM achieves crosstalk artifact suppression comparable to that of C-RTMM [Fig. 6(c)].

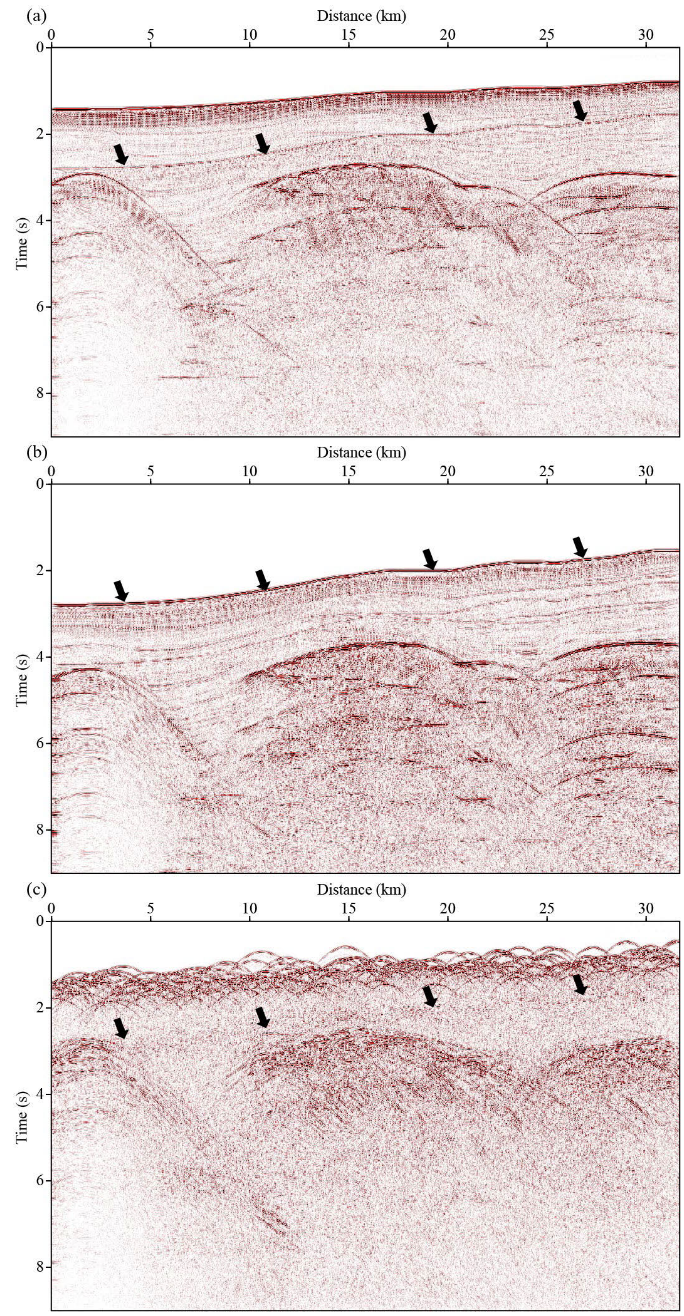

Fig. 9. Plane-wave gathers with a zero take-off angle (a) original data, (b) all-order multiples, and (c) forward-propagated supergathers. As indicated by the black arrows in (c), the first-order multiples exhibit randomized energy after applying the hybrid encoding.

areal source for forward wavefield propagation, while the other [Fig. 7(b)] is backward propagated to rebuild the receiver-side wavefield.

The PE-RTMM imaging result is displayed in Fig. 8. Compared with the RTMM image in Fig. 6(b), PE-RTMM effectively suppresses most crosstalk artifacts, as highlighted by the arrows. Its overall image quality is comparable to that of C-RTMM [Fig. 6(c)]. These results demonstrate that PE-RTMM retains the crosstalk-attenuation capability of C-RTMM while reducing the computational cost to approximately $1/N_m$ of that required by C-RTMM ($N_m = 3$ in this experiment).

Despite these advantages, PE-RTMM still operates in the shot domain, with each shot gather migrated independently and subsequently stacked. As a result, shot-domain migrations (e.g., RTM, RTMM, C-RTMM, and PE-RTMM) retain computationally demanding when applied to datasets containing a large number of shots. In the following subsections, we extend multiple imaging to the plane-wave domain to further enhance computational efficiency while maintaining effective crosstalk suppression.

D. Generation of Plane-Wave Gathers for Imaging With Multiples

By applying linear time-delay encoding, shot-domain data are transformed into plane-wave gathers, enabling multiple imaging in the plane-wave domain. Fig. 9(a)–(c) shows zero take-off-angle plane-wave gathers generated from the original data [Fig. 5(a)], the all-order multiples [Fig. 5(b)], and the forward-propagating supergather [Fig. 7(a)], respectively. As indicated by the black arrows in Fig. 9(a) and (b), first-order multiples from different shots remain coherent after plane-wave encoding using (15). This coherence leads to strong crosstalk artifacts in the corresponding images. In contrast, the plane-wave gather constructed from the supergather [Fig. 9(c)], encoded using (20), exhibits randomized multiple energy. This randomization effectively mitigates crosstalk among different multiple orders. Fig. 10(a) and (b) presents the imaging results obtained using PW-RTMM and HE-RTMM, respectively, with only the zero take-off-angle plane-wave gather. Both images show poor resolution of steep salt boundaries and deep structures, resulting in a low SNR. Nevertheless, HE-RTMM clearly suppresses the crosstalk artifacts caused by chaotic interactions among multiple orders in PW-RTMM, as highlighted by the green arrows.

The selection of the ray-parameter range and the number of ξ values plays a critical role in balancing imaging accuracy and computational efficiency. The ξ range should be carefully defined to ensure sufficient illumination of steeply dipping

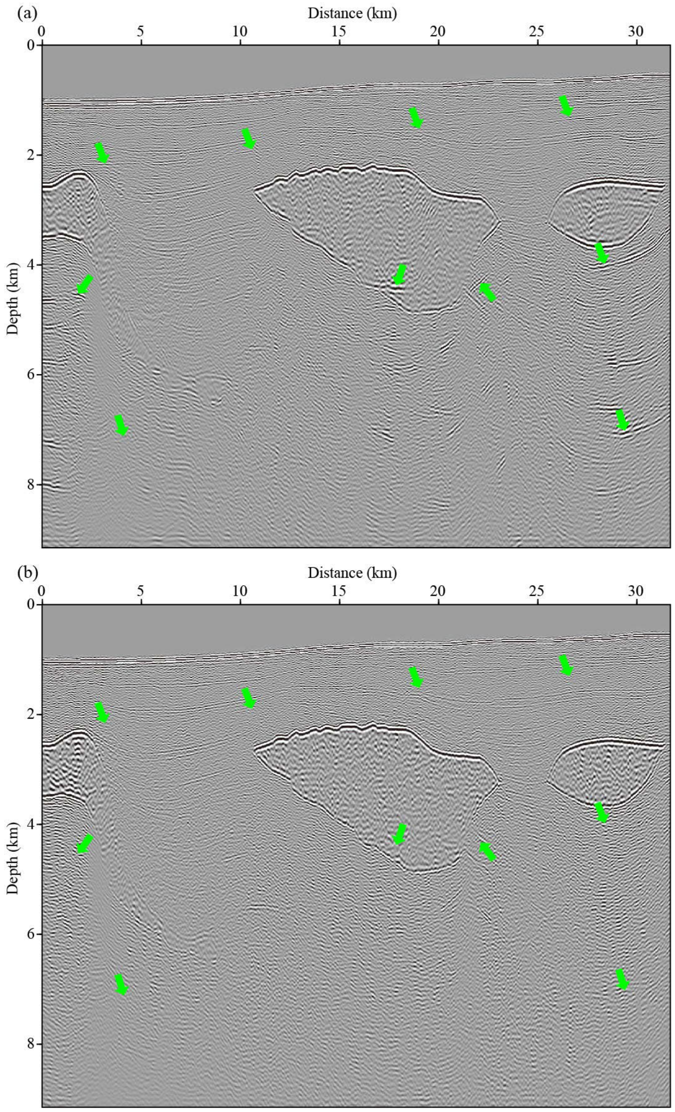

Fig. 10. Imaging results obtained using (a) PW-RTMM and (b) HE-RTMM with only one take-off angle (ξ = 0). Although the steep salt boundaries and deep structures are not well recovered, HE-RTMM clearly reduces the crosstalk artifacts present in PW-RTMM, as indicated by the arrows.

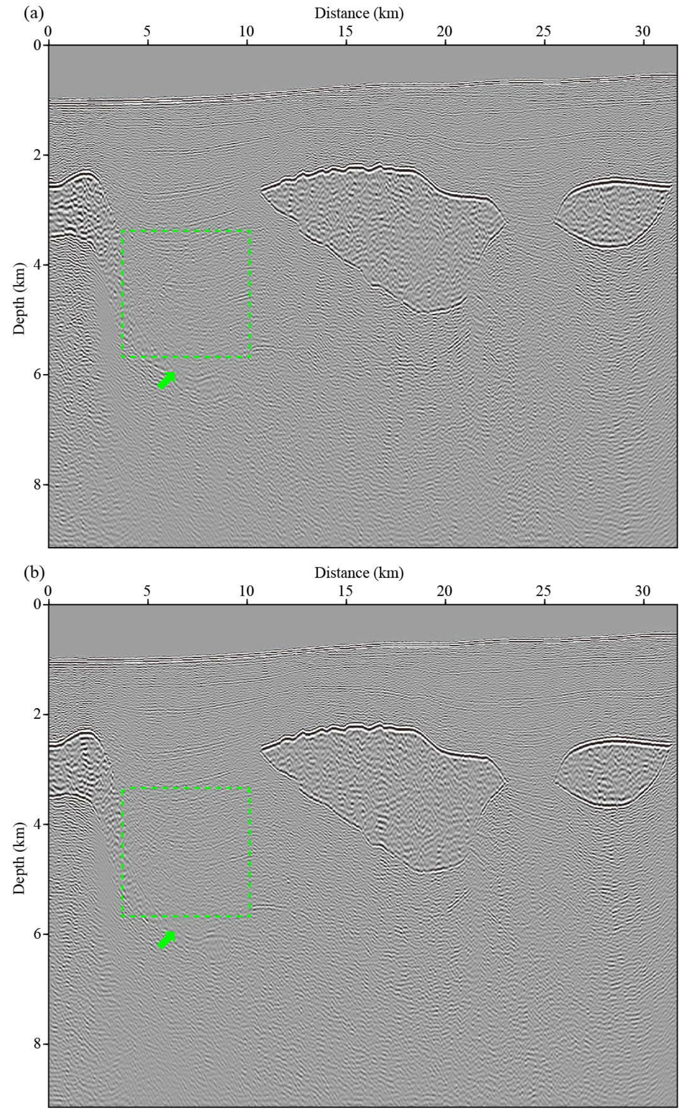

Fig. 11. Imaging results obtained using HE-RTMM with ξ value of (a) 0.216 and (b) 0.288 ms/m. As indicated by the rectangle and arrow, the image quality degrades as ξ increases. Thereby, 0.216 ms/m is selected as the ray-parameter boundary for plane-wave migration.

structures within the target area [40]. To investigate this effect, we performed prestack migration tests using several large ξ values. For the Pluto 1.5 model, imaging results obtained using HE-RTMM with ξ = 0.216 ms/m and ξ = 0.288 ms/m are shown in Fig. 11(a) and (b), respectively. The image in Fig. 11(a) fails to adequately illuminate the steep salt boundaries and deeper structures. As indicated by the rectangle, the image quality further degrades in Fig. 11(b), where structural coherence is noticeably reduced (see the arrow). Based on these observations, we adopted a ray-parameter range from −0.216 to 0.216 ms/m in subsequent experiments. Theoretical sampling criteria for take-off angles, which account for factors such as velocity model, reflector dipping angles, and recording aperture, were discussed by Zhang et al. [38]. In practice, however, the number of ray parameters used in industrial applications is often smaller than that prescribed by theory [37], [47], [48]. Following the recommendation of Dai and Schuster [43], we therefore selected 31 ξ values for plane-wave migration in this study.

E. Performance of the Proposed He-RTMM

In this section, we evaluate the performance of the proposed HE-RTMM using 31 plane-wave gathers with a ray-parameter sampling interval of 14.4 μs/m. When PW-RTMM is directly applied to the plane-wave gathers constructed from the original data and all-order multiples, the resulting image [Fig. 12(a)] contains abundant crosstalk artifacts. These artifacts are similar to those observed in the RTMM result [Fig. 6(b)]. These spurious events arise from cross-correlations between nonconsecutive multiple orders in the plane-wave domain and severely contaminate the true subsurface reflectors. In contrast, when shot gathers corresponding to individual multiple orders are first hybrid-encoded using (20), and HE-RTMM is then performed on the resulting plane-wave gathers, the migrated image [Fig. 12(b)] is largely free of such crosstalk artifacts. A direct comparison between the two images in Fig. 12 demonstrates that the proposed hybrid-encoding strategy effectively suppresses apparent crosstalk while preserving the main geological structures.

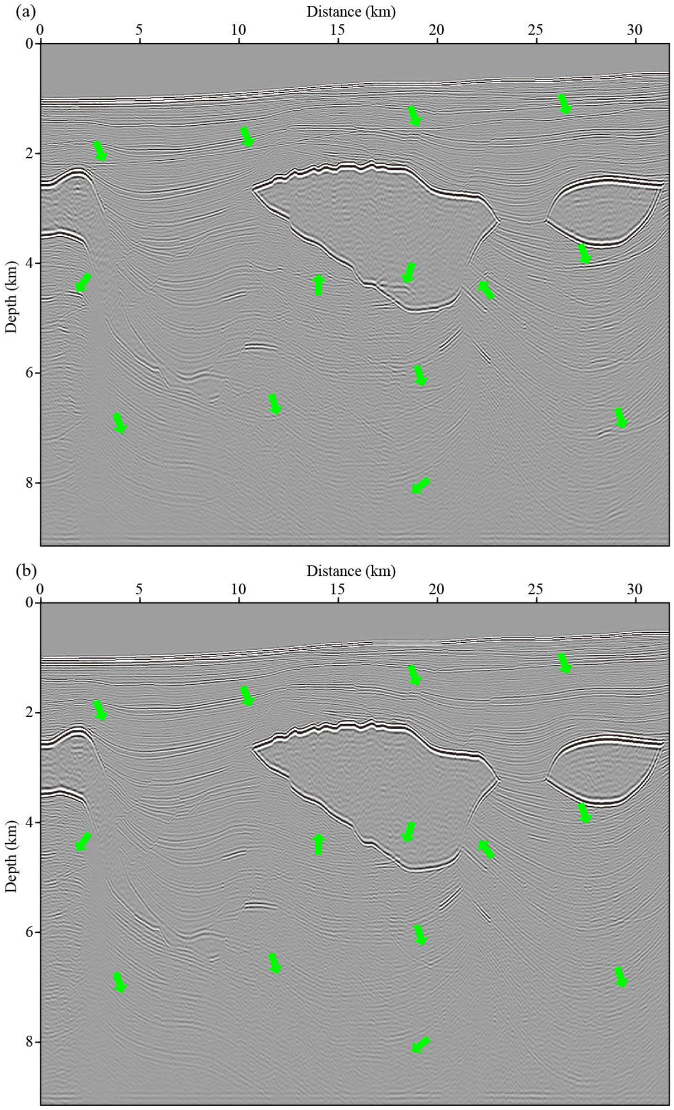

Fig. 12. Imaging results obtained using (a) PW-RTMM and (b) HE-RTMM with 31 take-off angles. The PW-RTMM image in (a) exhibits artifacts, as indicated by the arrows, which are effectively suppressed by the proposed HE-RTMM, as shown in (b).

To further illustrate the reduction of crosstalk artifacts, enlarged views of the subsalt regions from Figs. 6, 8, and 12 are shown in Fig. 13. Using the primary-only RTM image [Fig. 13(a)] as a reference, the C-RTMM result [Fig. 13(c)] successfully removes both insalt and subsalt crosstalk artifacts compared with the RTMM image [Fig. 13(b)]. This comparison confirms the superior imaging fidelity of C-RTMM. However, C-RTMM achieves this improvement at the expense of increased computational cost, which scales linearly with the number of multiple orders N_m. Nevertheless, C-RTMM achieves this improvement by reducing the migration cost by a factor of N_m. Although minor random noise remains, PE-RTMM [Fig. 13(d)] inherits the benefits of C-RTMM in crosstalk attenuation while reducing the computational cost to a level comparable to that of RTM or RTMM. Nevertheless, these shot-domain implementations remain computationally intensive because each shot must be migrated independently and subsequently stacked. Plane-wave migration offers a promising alternative for improving computational efficiency.

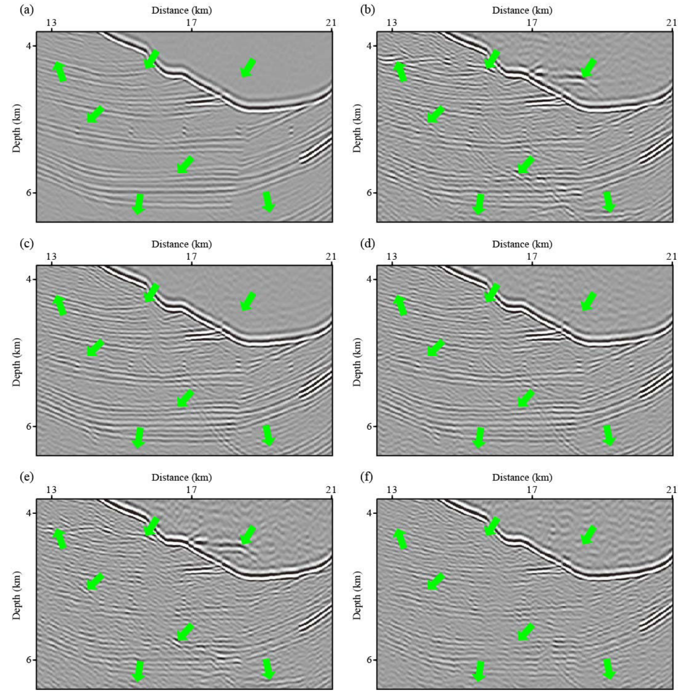

Fig. 13. Zoomed-in views of imaging results obtained using (a) RTM [Fig. 6(a)], (b) RTMM [Fig. 6(b)], (c) C-RTMM [Fig. 6(c)], (d) PE-RTMM (Fig. 8), (e) PW-RTMM [Fig. 12(a)], and (f) HE-RTMM [Fig. 12(b)]. The RTMM image in (b) and PW-RTMM image in (e) exhibit numerous artifacts, as indicated by the arrows, which are effectively suppressed by C-RTMM in (c), PE-RTMM in (d), and the proposed HE-RTMM in (f).

However, similar to shot-domain RTMM, directly migrating multiples in the plane-wave domain still generates coherent crosstalk artifacts, as indicated by the arrows in Fig. 13(e). In contrast, the proposed HE-RTMM effectively suppresses these artifacts, yielding an image with an improved SNR [Fig. 13(f)].

Both theoretical analyses and numerical experiments demonstrate that C-RTMM provides the most accurate multiple-based imaging results. Therefore, the C-RTMM image is used as the benchmark for evaluating the image quality of RTMM [Fig. 6(b)], PE-RTMM (Fig. 8), PW-RTMM [Fig. 12(a)], and HE-RTMM [Fig. 12(b)], as shown in Fig. 14. For a visual comparison, we employ the similarity coefficient criterion (SCC), also referred to as normalized cross-correlation

$$\mathrm{SCC}[x, y] = \frac{\sum_{i=1}^{N} x_i(t) y_i(t)}{\sqrt{\sum_{i=1}^{N} x_i^2(t) \sum_{i=1}^{N} y_i^2(t)}} \quad (25)$$

where $x_i(t)$ and $y_i(t)$ are the benchmark trace and the trial trace, respectively, N is the window size involved in the correlation computation (with $N = 1$ assumed in this comparison), and $\mathrm{SCC}[x, y]$ represents the correlation coefficient between the ith trial trace and the standard trace.

Fig. 14 shows the resulting similarity maps. All methods recover the main structural features of the model. However, RTMM and PW-RTMM exhibit extensive regions of coherent negative SCC values, indicating strong crosstalk from nonconsecutive multiple orders. For example, the arrows highlight the previously discussed spurious events parallel to the seafloor, while the rectangles mark the subsalt structural regions. In contrast, negative SCC values in PE-RTMM and HE-RTMM are more randomly distributed, reflecting their improved ability

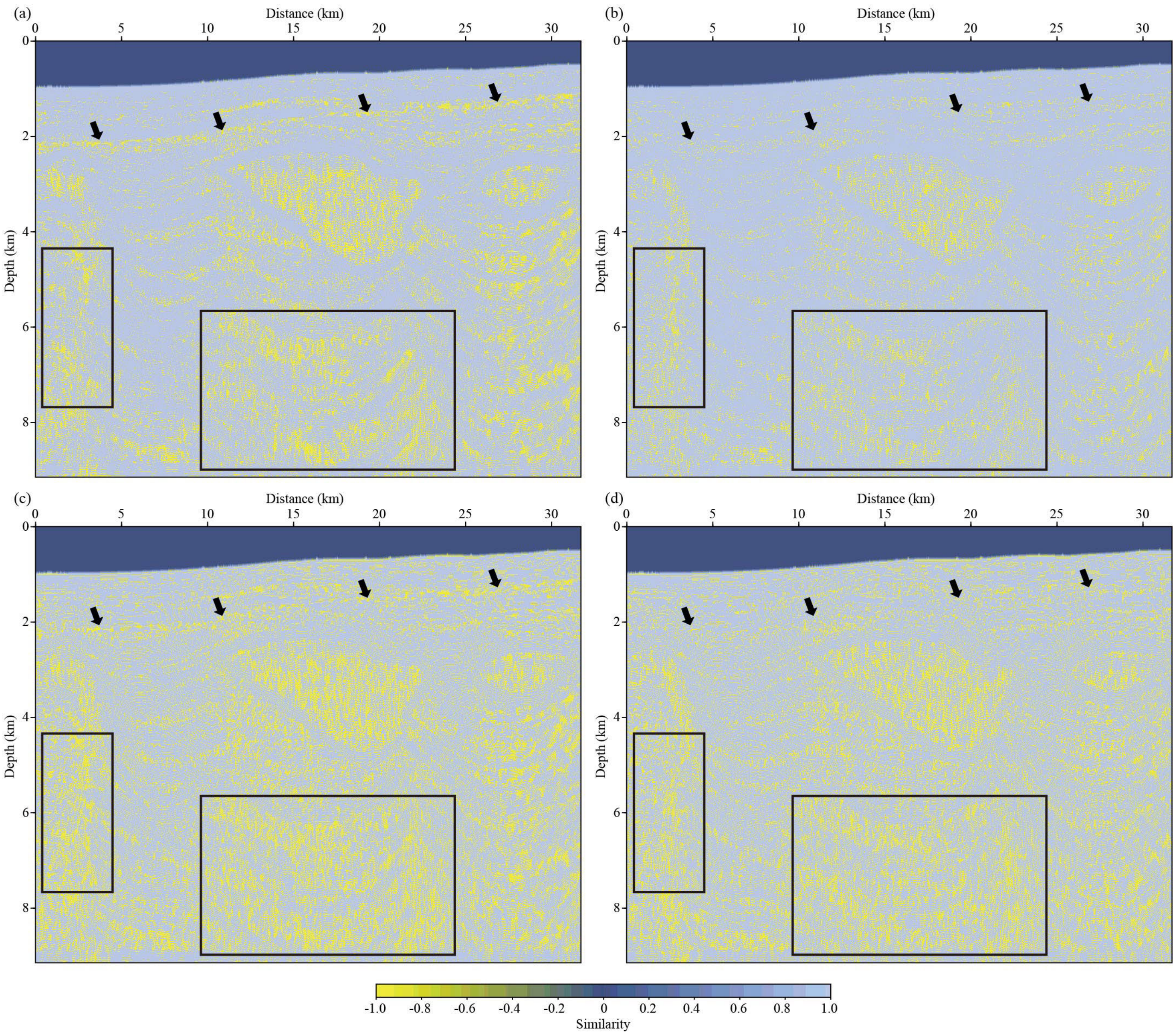

Fig. 14. Similarity of imaging results with respect to the C-RTMM image [Fig. 6(c)] (a) RTMM [Fig. 6(b)], (b) PE-RTMM (Fig. 8), (c) PW-RTMM [Fig. 12(a)], and (d) proposed HE-RTMM [Fig. 12(b)]. Coherent negative SCC values (yellow) indicate strong crosstalk. The black arrows and rectangles in (a) and (c) highlight the spurious events, which are effectively suppressed by PE-RTMM in (b) and by the proposed HE-RTMM in (d).

TABLE I

NORMALIZED COMPARISON OF COMPUTATIONAL COSTS OF DIFFERENT MIGRATION METHODS FOR THE PLUTO MODEL

	RTM	RTMM	C-RTMM	PE-RTMM	PW-RTMM	HE-RTMM
Migration-aperture ratio	1	1	1	1	1.901	1.901
Gather-number ratio	1	1	3	1	0.067	0.067
Data-duration ratio	1	1	1	1.052	1.380	1.432
Normalized computation cost	1	1	3	1.052	0.176	0.182

to suppress coherent crosstalk. Finally, comparisons between Fig. 14(a) and (c), as well as between Fig. 14(b) and (d), indicate that plane-wave-domain images generally exhibit a lower SNR than their shot-domain counterparts. This reduction arises because plane-wave migration employs a limited range of take-off angles, whereas shot-domain methods employ effectively infinite take-off angles, providing broader subsurface illumination.

F. Computational Cost Estimation

Table I summarizes the computational cost of different migration methods, normalized to that of shot-domain primary-only RTM. The cost of each method is estimated as the product of three relative factors: the migration-aperture ratio, the gather-number ratio, and the data-duration ratio, all referenced to shot-domain RTM.

In general, plane-wave RTMs are performed over the entire model, whereas shot-domain RTMs are confined to a finite migration aperture encompassing the source location and receiver spread. Taking into account the sponge absorbing layers used during wavefield propagation, the effective migration aperture in the plane-wave domain is approximately (1387+400)/(540+400) $\approx$ 1.901 times that of the shot-domain cases in our experiments. For plane-wave migrations, 31 plane-wave gathers are constructed from 463 shot gathers. This configuration yields a gather-number ratio of 31/463 $\approx$ 0.067.

The data-duration ratio depends on the encoding strategy. According to (12), the duration of a supergather equals the original time length plus a time shift. Because the time shifts are randomly assigned, we use their standard deviation (0.467 s) as a representative time increment for uniform processing. Given a shot-gather recording time of 9 s, the resulting duration ratio for PE-RTMM is approximately $(9 + 0.467)/9 \approx 1.052$. In plane-wave migration, linear time delays are accumulated across shot gathers to form each plane-wave gather. The duration of a plane-wave gather therefore depends on the ray parameter. To estimate the average delay, we multiply the mean absolute ray parameter (0.108 ms/m) by the source-array length (31.68 km), which yields an average delay of 3.421 s. Consequently, the average duration ratio for PW-RTMM is approximately $(9 + 3.421)/9 \approx 1.380$. When both random-phase encoding and linear time-delay encoding are applied, the combined duration ratio of HE-RTMM becomes $(9 + 0.467 + 3.421)/9 \approx 1.432$.

For shot-domain migrations, the computational costs of primary-only RTM [Fig. 6(a)] and RTMM [Fig. 6(b)] are identical. To produce the C-RTMM image shown in Fig. 6(c), the first three multiple orders are migrated independently, resulting in a total cost three times that of RTM. The PE-RTMM image (Fig. 8) requires a computational cost approximately 1.052 times that of RTM. By multiplying the gather-number, migration-aperture, and data-duration ratios, the computational cost of PW-RTMM [Fig. 12(a)] is estimated as $0.067 \times 1.901 \times 1.380 \approx 0.176$. Similarly, the cost of HE-RTMM [Fig. 12(b)] is approximately $0.067 \times 1.901 \times 1.432 \approx 0.182$. Compared with PW-RTMM, the proposed HE-RTMM achieves effective crosstalk suppression with only a marginal increase in computational cost.

IV. Discussion

Conventional migration algorithms usually treat multiples as noise and suppress them prior to imaging. However, multiples are also true seismic reflections that travel along longer propagation paths. As a result, they can provide broader subsurface illumination than primaries and help recover structural details in regions that are poorly illuminated by primaries alone. Imaging with multiples therefore offers a valuable opportunity to enhance subsurface characterization.

A major challenge in multiple imaging is the presence of coherent crosstalk artifacts. These artifacts arise from cross-correlations between multiples of nonconsecutive or chaotic orders. They can significantly degrade image quality by smearing structural features, reducing resolution, and potentially leading to erroneous geological interpretations. Migrating multiples in an order-by-order manner effectively suppresses such crosstalk. However, this strategy increases the computational cost by a factor of N_m relative to conventional shot-domain migrations. To balance crosstalk suppression and computational efficiency, we propose a plane-wave-based multiple migration method, termed HE-RTMM. This approach integrates random-phase encoding with plane-wave encoding, enabling efficient multiple imaging while preserving effective crosstalk attenuation.

Despite the encouraging theoretical analysis and numerical results, the proposed method has several limitations. Similar to C-RTMM, HE-RTMM strongly depends on the accuracy of multiple-order decomposition. When the separation is imperfect, such as that caused by low-data SNR, residual energy from unrelated chaotic orders may persist in both the forward- and backward-propagated wavefields. This residual energy can generate coherent crosstalk artifacts [24], [25]. As the decomposition quality deteriorates, the image produced by HE-RTMM [Fig. 12(b)] gradually degrades and approaches the quality of PW-RTMM [Fig. 12(a)].

Another important limitation arises from the plane-wave migration itself. As shown in Fig. 14, plane-wave migrations generally exhibit lower SNR than shot-domain migrations due to aliasing artifacts. Zhang et al. [38] demonstrated that discretization errors in plane-wave migration can be evaluated by comparing the original wavefield with its filtered version. When the ray-parameter sampling does not satisfy the theoretical sampling criterion, the wavefield becomes undersampled, leading to aliasing noise in the migrated images. Increasing the range and number of ray parameters can alleviate these artifacts and improve image quality, as evidenced by the comparison between Figs. 10(b) and 12(b). Nevertheless, plane-wave migration inherently involves a trade-off between aliasing suppression and computational efficiency. Simply increasing the number of take-off angles is therefore not always cost-effective [38], [47].

These limitations become more pronounced when seismic data are contaminated by noise, as is often the case for field datasets. In such scenarios, inversion-based imaging provides an effective mitigation strategy. Among these methods, least-squares migration (LSM) is particularly attractive. As a linear inversion framework, LSM iteratively reduces imaging artifacts while enhancing spatial resolution [49], [50], [51]. Extending this idea, least-squares RTMM incorporates the RTMM operator into the LSM formulation, allowing iterative suppression of multiple-related crosstalk [52], [53], [54], [55], [56]. This inversion-based approach not only improves multiple-imaging fidelity but also enhances robustness to noise in real-data applications.

In parallel, recent advances in deep learning offer additional opportunities to improve plane-wave-based imaging. Convolutional neural network (CNN)-based methods have shown strong potential for suppressing aliasing noise and enhancing migration results. For example, Li et al. [57] proposed a deep-learning-based image denoising technique that enables high-quality plane-wave migration using only seven angles. Beyond image-domain enhancement, CNN-based postprocessing can also be applied directly to seismic data to improve data SNR [58], which in turn benefits plane-wave migration results. These developments suggest promising directions for improving HE-RTMM and enhancing its robustness in future studies.

V. Conclusion

During multiple migrations, cross-correlations between nonconsecutive multiple orders generate coherent crosstalk artifacts that severely degrade image fidelity. Migrating multiples in an order-to-order manner can effectively suppress these artifacts. However, when all multiple orders are migrated in the shot domain, the computational cost becomes prohibitively high. To overcome this limitation, we propose a computationally efficient migration strategy that converts hundreds of shot-domain gathers into only dozens of plane-wave gathers using a hybrid-encoding scheme. This scheme combines random-phase encoding and linear time-delay encoding. Random-phase encoding is applied across different multiple orders to suppress crosstalk, while linear time-delay encoding significantly reduces the number of gathers required for migration. Numerical experiments on the Pluto 1.5 model demonstrate that the proposed method effectively attenuates coherent crosstalk artifacts while substantially improving computational efficiency compared with conventional shot-domain RTM-based multiple imaging. In addition, aliasing artifacts can be further mitigated by increasing the number of ray parameters or by incorporating inversion-based or deep-learning-based imaging optimization techniques.

Appendix
Workflow for Decomposing Multiples Into Different Orders

As an effective approach for multiple attenuation, the SRME algorithm has been widely applied in both industry and academic research [1]. Based on a feedback model, SRME predicts all orders of surface-related multiples through the frequency-domain self-product of the originally recorded data $\mathbf{G}$

$$\mathbf{G}'_m = \mathbf{G}\mathbf{G}. \tag{A.1}$$

Here, $\mathbf{G}'_m$ denotes the predicted all-order multiples. Then, $\mathbf{G}'_m$ are adaptively subtracted from $\mathbf{G}$ to obtain the primaries $\mathbf{G}_0$

$$\mathbf{G}_0 = \mathbf{G} - \mathbf{G}_m \tag{A.2}$$

where $\mathbf{G}_m = \boldsymbol{\gamma}\mathbf{G}'_m$ denote the estimated all-order multiples and $\boldsymbol{\gamma}$ is an adaptive filtering factor. However, direct application of SRME cannot yield separated multiple orders. To address this, we reformulate the prediction and subtraction processing as follows:

$$\begin{cases} \boldsymbol{\Phi}_{i+1} = \mathbf{G}_0\boldsymbol{\Phi}_i \\ \mathbf{G}_i = \boldsymbol{\Phi}_i - \boldsymbol{\gamma}\boldsymbol{\Phi}_{i+1} \end{cases} \tag{A.3}$$

where $\boldsymbol{\Phi}_i = \sum_{j=i}^{N_m} \mathbf{G}_j$ represents the data containing multiples with order equal to or higher than i, and $\mathbf{G}_j$ denotes the jth-order multiples. By iteratively applying (A.3), any specific order of multiples can be extracted. For example, when $i = 1$, the first-order multiples $\mathbf{G}_1$ can be acquired by subtracting $\boldsymbol{\Phi}_2$ from $\boldsymbol{\Phi}_1$.

References

[1] D. J. Verschuur, A. J. Berkhout, and C. P. A. Wapenaar, "Adaptive surface-related multiple elimination," *Geophysics*, vol. 57, no. 9, pp. 1166–1177, Sep. 1992. [Online]. Available: https://pubs.geoscienceworld.org/geophysics/article/57/9/1166/106391/Adaptive-surface-related-multiple-elimination

[2] T. Wang, D. Wang, J. Sun, and B. Hu, "Passive seismic data primary estimation and noise removal via focal-denoising closed-loop surface-related multiple elimination based on 3D L1-norm sparse inversion," *Geophys. Prospecting*, vol. 69, no. 1, pp. 122–138, Jan. 2021. [Online]. Available: https://onlinelibrary.wiley.com/doi/10.1111/1365-2478.13034

[3] D. J. Foster and C. C. Mosher, "Suppression of multiple reflections using the radon transform," *Geophysics*, vol. 57, no. 3, pp. 386–395, Mar. 1992. [Online]. Available: https://pubs.geoscienceworld.org/geophysics/article/57/3/386/72694/Suppression-of-multiple-reflections-using-the

[4] Y. Wang, "Multiple attenuation: Coping with the spatial truncation effect in the radon transform domain," *Geophys. Prospecting*, vol. 51, no. 1, pp. 75–87, Jan. 2003. [Online]. Available: https://onlinelibrary.wiley.com/doi/10.1046/j.1365-2478.2003.00355.x

[5] M. P. Brown and A. Guitton, "Least-squares joint imaging of multiples and primaries," *Geophysics*, vol. 70, no. 5, pp. S79–S89, Jan. 2005. [Online]. Available: https://pubs.geoscienceworld.org/geophysics/article/70/5/S79/251333/Least-squares-joint-imaging-of-multiples-and

[6] A. J. Berkhout and D. J. Verschuur, "Imaging of multiple reflections," *Geophysics*, vol. 71, no. 4, pp. SI209–SI220, Jan. 2006. [Online]. Available: https://pubs.geoscienceworld.org/geophysics/article/71/4/SI209/107321/Imaging-of-multiple-reflectionsImaging-of-multiple

[7] R. Muijs, A. J. O. Robertsson, and K. Holliger, "Prestack depth migration of primary and surface-related multiple reflections: Part I—Imaging," *Geophysics*, vol. 72, no. 2, pp. S59–S69, Jan. 2007. [Online]. Available: https://pubs.geoscienceworld.org/geophysics/article/72/2/S59/262213/Prestack-depth-migration-of-primary-and-surface

[8] Z. Jiang, J. Sheng, J. Yu, G. T. Schuster, and B. E. Hornby, "Migration methods for imaging different-order multiples," *Geophys. Prospecting*, vol. 55, no. 1, pp. 1–19, Jan. 2007. [Online]. Available: https://onlinelibrary.wiley.com/doi/10.1111/j.1365-2478.2006.00598.x

[9] Y. Liu, X. Chang, D. Jin, R. He, H. Sun, and Y. Zheng, "Reverse time migration of multiples for subsalt imaging," *Geophysics*, vol. 76, no. 5, pp. WB209–WB216, Sep. 2011. [Online]. Available: https://pubs.geoscienceworld.org/geophysics/article/76/5/WB209/308391/Reverse-time-migration-of-multiples-for-subsalt

[10] A. Zuberi and T. Alkhalifah, "Imaging by forward propagating the data: Theory and application," *Geophys. Prospecting*, vol. 61, no. s1, pp. 248–267, Jun. 2013. [Online]. Available: https://onlinelibrary.wiley.com/doi/10.1111/1365-2478.12006

[11] A. Ordoñez, W. Söllner, T. Klüver, and L. J. Gelius, "Migration of primaries and multiples using an imaging condition for amplitude-normalized separated wavefields," *Geophysics*, vol. 79, no. 5, pp. S217–S230, Sep. 2014. [Online]. Available: https://pubs.geoscienceworld.org/geophysics/article/79/5/S217/284949/Migration-of-primaries-and-multiples-using-an

[12] Y. Wang, Y. Zheng, L. Zhang, X. Chang, and Z. Yao, "Reverse time migration of multiples: Eliminating migration artifacts in angle domain common image gathers," *Geophysics*, vol. 79, no. 6, pp. S263–S270, Nov. 2014. [Online]. Available: https://pubs.geoscienceworld.org/geophysics/article/79/6/S263/273752/Reverse-time-migration-of-multiples-Eliminating

[13] S. Lu, D. N. Whitmore, A. A. Valenciano, and N. Chemingui, "Separated-wavefield imaging using primary and multiple energy," *Lead. Edge*, vol. 34, no. 7, pp. 770–778, Jul. 2015. [Online]. Available: https://pubs.geoscienceworld.org/tle/article/34/7/770/136600/Separated-wavefield-imaging-using-primary-and

[14] N. Tu and F. J. Herrmann, "Fast imaging with surface-related multiples by sparse inversion," *Geophys. J. Int.*, vol. 201, no. 1, pp. 304–317, Apr. 2015. [Online]. Available: http://academic.oup.com/gji/article/201/1/304/733341/Fast-imaging-with-surfacerelated-multiples-by

[15] Y. Qu, C. Huang, C. Liu, and Z. Li, "Full-path compensated least-squares reverse time migration of joint primaries and different-order multiples for deep-marine environment," *IEEE Trans. Geosci. Remote Sens.*, vol. 59, no. 8, pp. 7109–7121, Aug. 2021. [Online]. Available: https://ieeexplore.ieee.org/document/9214896/

[16] Z. Li et al., "Artifact suppression for the joint imaging of primaries and internal multiples," *IEEE Trans. Geosci. Remote Sens.*, vol. 60, 2022, Art. no. 5919509. [Online]. Available: https://ieeexplore.ieee.org/document/9858886/

[17] S. Zhang, S. Lu, X. Dong, and K. Ren, "Angle-domain common-image gathers for imaging of multiples using Poynting vectors," *IEEE Trans. Geosci. Remote Sens.*, vol. 61, 2023, Art. no. 5903613. [Online]. Available: https://ieeexplore.ieee.org/document/10043751/

[18] E. Baysal, D. Kosloff, and J. W. C. Sherwood, "Reverse time migration," *Geophysics*, vol. 48, no. 11, pp. 1514–1524, Nov. 1983. [Online]. Available: https://pubs.geoscienceworld.org/geophysics/article/48/11/1514/68712/Reverse-time-migration

[19] H.-W. Zhou, H. Hu, Z. Zou, Y. Wo, and O. Youn, "Reverse time migration: A prospect of seismic imaging methodology," *Earth-Sci. Rev.*, vol. 179, pp. 207–227, Apr. 2018. [Online]. Available: https://linkinghub.elsevier.com/retrieve/pii/S0012825217306256

[20] Y. Zheng and Y. Wang, "High-resolution reflection seismic imaging to reveal subsurface geologic structures of a deep geothermal reservoir," *Geophysics*, vol. 88, no. 5, pp. WB37–WB43, Sep. 2023. [Online]. Available: https://pubs.geoscienceworld.org/geophysics/article/88/5/WB37/624258/High-resolution-reflection-seismic-imaging-to

[21] L. Ren, Q. Du, W. Lv, W. Wu, and T. Jan Moser, "Vector decoupling-based elastic reverse time migration for OBN data in VTI media," *IEEE Trans. Geosci. Remote Sens.*, vol. 63, 2025, Art. no. 5921410. [Online]. Available: https://ieeexplore.ieee.org/document/11151296/

[22] J. Sun, Z. Zhao, J. Ma, and J. Yang, "Elastic wavefield decomposition using the physical-constrained neural network and its application on reverse-time migration," *IEEE Trans. Geosci. Remote Sens.*, vol. 63, 2025, Art. no. 4505811. [Online]. Available: https://ieeexplore.ieee.org/document/11007264/

[23] X. Liu, Y. Liu, H. Hu, P. Li, and M. Khan, "Imaging of first-order surface-related multiples by reverse-time migration," *Geophys. J. Int.*, vol. 208, no. 2, pp. 1077–1087, Feb. 2017. [Online]. Available: https://academic.oup.com/gji/article-lookup/doi/10.1093/gji/ggw437

[24] Y. Zhang, Y. Liu, X. Liu, and X. Zhou, "Reverse time migration using waterbottomrelated multiples," *Geophys. Prospecting*, vol. 68, no. 2, pp. 446–465, Feb. 2020. [Online]. Available: https://onlinelibrary.wiley.com/doi/10.1111/1365-2478.12851

[25] Y. Liu, X. Liu, A. Osen, Y. Shao, H. Hu, and Y. Zheng, "Least-squares reverse time migration using controlled-order multiple reflections," *Geophysics*, vol. 81, no. 5, pp. S347–S357, Sep. 2016. [Online]. Available: https://pubs.geoscienceworld.org/geophysics/article/81/5/S347/432018/Least-squares-reverse-time-migration-using

[26] Z. Li, Z. Li, P. Wang, and M. Zhang, "Reverse time migration of multiples based on different-order multiple separation," *Geophysics*, vol. 82, no. 1, pp. S19–S29, Jan. 2017. [Online]. Available: https://pubs.geoscienceworld.org/geophysics/article/82/1/S19/283277/Reverse-time-migration-of-multiples-based-on

[27] Y. Qu, J. Li, Z. Guan, and Z. Li, "Viscoacoustic reverse time migration of joint primaries and different-order multiples," *GEOPHYSICS*, vol. 85, no. 2, pp. S71–S87, Mar. 2020. [Online]. Available: https://library.seg.org/doi/10.1190/geo2019-0237.1

[28] L. A. Romero, D. C. Ghiglia, C. C. Ober, and S. A. Morton, "Phase encoding of shot records in prestack migration," *Geophysics*, vol. 65, no. 2, pp. 426–436, Jan. 2000. [Online]. Available: https://pubs.geoscienceworld.org/geophysics/article/65/2/426/73592/Phase-encoding-of-shot-records-in-prestack

[29] G. T. Schuster, X. Wang, Y. Huang, W. Dai, and C. Boonyasiriwat, "Theory of multisource crosstalk reduction by phase-encoded statics: Theory of multisource crosstalk reduction," *Geophys. J. Int.*, vol. 184, no. 3, pp. 1289–1303, Mar. 2011. [Online]. Available: https://academic.oup.com/gji/article-lookup/doi/10.1111/j.1365-246X.2010.04906.x

[30] P. Zhang, L. Han, X. Gong, H. Sun, and B. Mao, "Multi-source elastic full waveform inversion based on the anisotropic total variation constraint," *Chin. J. Geophys.*, vol. 2, no. 61, pp. 716–732, Feb. 2018.

[31] J. R. Krebs et al., "Fast full-wavefield seismic inversion using encoded sources," *Geophysics*, vol. 74, no. 6, pp. WCC177–WCC188, Jan. 2009. [Online]. Available: https://pubs.geoscienceworld.org/geophysics/article/74/6/WCC177/303706/Fast-full-wavefield-seismic-inversion-using

[32] W. Dai, P. Fowler, and G. T. Schuster, "Multisource leastsquares reverse time migration," *Geophys. Prospecting*, vol. 60, no. 4, pp. 681–695, Jul. 2012. [Online]. Available: https://onlinelibrary.wiley.com/doi/10.1111/j.1365-2478.2012.01092.x

[33] X. Liu, Y. Liu, and M. Khan, "Fast least-squares reverse time migration of VSP free-surface multiples with dynamic phase-encoding schemes," *Geophysics*, vol. 83, no. 4, pp. S321–S332, Jul. 2018. [Online]. Available: https://library.seg.org/doi/10.1190/geo2017-0419.1

[34] Y. Liu, Y. Zhang, and Y. Zheng, "Reverse time migration of phase-encoded all-order multiples," *Geophysics*, vol. 87, no. 2, pp. S45–S52, Mar. 2022. [Online]. Available: https://pubs.geoscienceworld.org/geophysics/article/87/2/S45/611157/Reverse-time-migration-of-phase-encoded-all-order

[35] Y. Zhang and Y. Liu, "Phase-encoding-based least-squares reverse time migration of controlled-order multiples," *Geophysics*, vol. 88, no. 3, pp. S101–S113, May 2023. [Online]. Available: https://pubs.geoscienceworld.org/geophysics/article/88/3/S101/621300/Phase-encoding-based-least-squares-reverse-time

[36] Y. Zhang, F. Hu, and Y. Hu, "Seismic migration of water-bottom-related multiples accelerated by random phase-encoding strategy," *Geophys. Prospecting*, vol. 72, no. 7, pp. 2634–2645, Sep. 2024. [Online]. Available: https://onlinelibrary.wiley.com/doi/10.1111/1365-2478.13552

[37] J. T. Etgen, "How many angles do we really need for delayed-shot migration?," *SEG Technical Program Expanded Abstracts*, pp. 1985–1988, Jan. 2005. [Online]. Available: https://library.seg.org/doi/10.1190/1.2148097

[38] Y. Zhang, J. Sun, C. Notfors, S. H. Gray, L. Chernis, and J. Young, "Delayed-shot 3D depth migration," *Geophysics*, vol. 70, no. 5, pp. E21–E28, Jan. 2005. [Online]. Available: https://library.seg.org/doi/10.1190/1.2146078

[39] F. Perrone and P. Sava, "Waveequation migration with dithered plane waves," *Geophys. Prospecting*, vol. 60, no. 3, pp. 444–465, May 2012. [Online]. Available: https://onlinelibrary.wiley.com/doi/10.1111/j.1365-2478.2011.01011.x

[40] C. Li, J. Huang, Z. Li, and R. Wang, "Plane-wave least-squares reverse time migration with a preconditioned stochastic conjugate gradient method," *Geophysics*, vol. 83, no. 1, pp. S33–S46, Jan. 2018. [Online]. Available: https://library.seg.org/doi/10.1190/geo2017-0339.1

[41] F. Liu, D. W. Hanson, N. D. Whitmore, R. S. Day, and R. H. Stolt, "Toward a unified analysis for source plane-wave migration," *Geophysics*, vol. 71, no. 4, pp. S129–S139, Jul. 2006. [Online]. Available: https://library.seg.org/doi/10.1190/1.2213933

[42] D. Vigh and E. W. Starr, "3D prestack plane-wave, full-waveform inversion," *Geophysics*, vol. 73, no. 5, pp. VE135–VE144, Jan. 2008. [Online]. Available: https://library.seg.org/doi/10.1190/1.2952623

[43] W. Dai and G. T. Schuster, "Plane-wave least-squares reverse-time migration," *Geophysics*, vol. 78, no. 4, pp. S165–S177, Jul. 2013. [Online]. Available: https://library.seg.org/doi/10.1190/geo2012-0377.1

[44] X. Liu and Y. Liu, "Plane-wave domain least-squares reverse time migration with free-surface multiples," *Geophysics*, vol. 83, no. 6, pp. S477–S487, Nov. 2018. [Online]. Available: https://library.seg.org/doi/10.1190/geo2017-0570.1

[45] R.-E. Plessix, "A review of the adjoint-state method for computing the gradient of a functional with geophysical applications," *Geophys. J. Int.*, vol. 167, no. 2, pp. 495–503, Nov. 2006. [Online]. Available: https://academic.oup.com/gji/article-lookup/doi/10.1111/j.1365-246X.2006.02978.x

[46] D. Stoughton, J. Stefani, and S. Michell, "2D elastic model for wavefield investigations of subsalt objectives, deep water Gulf of Mexico," *SEG Tech. Program Expanded Abstracts*, pp. 1269–1272, Jan. 2001. [Online]. Available: http://library.seg.org/doi/abs/10.1190/1.1816325

[47] C. Stork and J. Kapoor, "How many p values do you want to migrate for delayed shot wave equation migration?," *SEG Tech. Program Expanded Abstracts*, pp. 1041–1044, Jan. 2004. [Online]. Available: https://library.seg.org/doi/10.1190/1.1843291

[48] Y. Zhang, J. Sun, C. Notfors, S. H. Gray, L. Chernis, and J. Young, "Reply to the discussion on 'delayed-shot 3D depth migration," *Geophysics*, vol. 71, no. 5, pp. X27–X29, Sep. 2006. [Online]. Available: https://library.seg.org/doi/10.1190/1.2335618

[49] T. Nemeth, C. Wu, and G. T. Schuster, "Least-squares migration incomplete reflection data," *Geophysics*, vol. 64, no. 1, pp. 208–221, Feb. 1999. [Online]. Available: https://pubs.geoscienceworld.org/geophysics/article/64/1/208/73432/Least-squares-migration-incomplete-reflection-data

[50] K. Yang and J. Zhang, "Comparison between born and Kirchhoff operators for least-squares reverse time migration and the constraint of the propagation of the background wavefield," *Geophysics*, vol. 84, no. 5, pp. R725–R739, Sep. 2019. [Online]. Available: https://pubs.geoscienceworld.org/geophysics/article/84/5/R725/573195/Comparison-between-Born-and-Kirchhoff-operators

[51] G. Peng, X. Gong, S. Lv, Z. Cao, Y. Nabi, and Z. Xu, "Regularization by denoising for the least-squares reverse time migration with source encoding," *IEEE Trans. Geosci. Remote Sens.*, vol. 63, 2025, Art. no. 5910015. [Online]. Available: https://ieeexplore.ieee.org/document/10947070/

[52] D. Zhang and G. T. Schuster, "Least-squares reverse time migration of multiples," *Geophysics*, vol. 79, no. 1, pp. S11–S21, Jan. 2014. [Online]. Available: https://pubs.geoscienceworld.org/geophysics/article/79/1/S11/308565/Least-squares-reverse-time-migration-of

[53] M. Wong, B. L. Biondi, and S. Ronen, "Imaging with primaries and free-surface multiples by joint least-squares reverse time migration," *Geophysics*, vol. 80, no. 6, pp. S223–S235, Nov. 2015. [Online]. Available: https://pubs.geoscienceworld.org/geophysics/article/80/6/S223/309226/Imaging-with-primaries-and-free-surface-multiples

[54] N. Tu and F. J. Herrmann, "Fast least-squares imaging with surface-related multiples: Application to a North Sea data set," *Lead. Edge*, vol. 34, no. 7, pp. 788–794, Jul. 2015. [Online]. Available: https://pubs.geoscienceworld.org/tle/article/34/7/788/136604/Fast-least-squares-imaging-with-surface-related
[55] Y. Zheng, Y. Wang, and X. Chang, "Least-squares data-to-data migration: An approach for migrating free-surface-related multiples," *Geophysics*, vol. 84, no. 2, pp. S83–S94, Mar. 2019. [Online]. Available: https://library.seg.org/doi/10.1190/geo2018-0080.1
[56] J. Li, Y. Qu, M. Li, and Z. Li, "Viscoacoustic leastsquares reversetime migration of differentorder freesurface multiples," *Geophys. Prospecting*, vol. 71, no. 1, pp. 29–47, Jan. 2023. [Online]. Available: https://onlinelibrary.wiley.com/doi/10.1111/1365-2478.13274
[57] Y. Li, X. Jia, X. Wu, and Z. Geng, "Deep learning for enhancing multisource reverse time migration," *IEEE Trans. Geosci. Remote Sens.*, vol. 60, 2022, Art. no. 4512313. [Online]. Available: https://ieeexplore.ieee.org/document/9889695/
[58] S. Sadrizadeh, H. Otroshi-Shahreza, and F. Marvasti, "Impulsive noise removal via a blind CNN enhanced by an iterative post-processing," *Signal Process.*, vol. 192, Mar. 2022, Art. no. 108378. [Online]. Available: https://linkinghub.elsevier.com/retrieve/pii/S0165168421004151

Baoqing Tian received the B.S. degree from China University of Mining and Technology, Xuzhou, China, in 2011, and the Ph.D. degree from the Institute of Geology and Geophysics, Chinese Academy of Sciences, Beijing, China, in 2017.

He is currently an Associate Professor with the Institute of Geophysics, China Earthquake Administration, Beijing. His research interests include seismic migration and microtremor survey.

Feng Hu received the B.S. degree from China University of Geosciences (Beijing), Beijing, China, in 2015, and the Ph.D. degree from the Institute of Geology and Geophysics, Chinese Academy of Sciences, Beijing, in 2021.

He is currently a Senior Engineer with Zhejiang Institute of Communications Company Ltd., Hangzhou, China. His research interests include microseismic monitoring technologies for landslide monitoring and early warning along highways.

Yanbao Zhang received the B.S. degree from Jilin University, Changchun, China, in 2015, and the Ph.D. degree from the Institute of Geology and Geophysics, Chinese Academy of Sciences, Beijing, China, in 2020.

He is currently an Associate Professor with the Institute of Geophysics, China Earthquake Administration, Beijing. His research interests include multiple imaging, multiple suppression, and least-squares migration.

Yike Liu received the B.S. degree from the Department of Physics, Peking University, Beijing, China, in 1982, and the Ph.D. degree from Chinese Academy of Sciences, Beijing, in 1998.

He is currently a Professor of geophysics with the Key Laboratory of Deep Petroleum Intelligent Exploration and Development, Institute of Geology and Geophysics, Chinese Academy of Sciences. His research interests include seismic propagation and imaging, seismic multiples attenuation and imaging, full-waveform inversion (FWI), and fracture detection.

Dr. Liu was a recipient of the 2022 SEG Reginald Fessenden Award for his landmark contributions in the development and application of seismic imaging using multiples. He was an Associate Editor of Geophysics.

Ning Wang (Member, IEEE) received the B.S. degree from Jilin University, Changchun, China, in 2015, and the Ph.D. degree from China University of Petroleum at Beijing (CUPB), Beijing, China, in 2020.

He is currently an Associate Professor with the School of Earth Science, Northeast Petroleum University, Daqing, China. His research interests include seismic wave propagation, reverse time migration, full-waveform inversion, and machine learning.

Jing Sun received the B.S. and M.S. degrees from Jilin University, Changchun, China, in 2015 and 2018, respectively, and the Ph.D. degree from the University of Oslo, Oslo, Norway, in 2022.

She is currently an Assistant Professor with the Intelligent Systems Department, Delft University of Technology, Delft, The Netherlands. Her research interests include machine learning for resolving geophysical challenges.